Monthly Notices
of the
ROYAL ASTRONOMICAL SOCIETY

Mon. Not. R. Astron. Soc. **416,** 832–856 (2011) doi:10.1111/j.1365-2966.2011.19054.x

The Australia Telescope Compact Array Broad-band Backend: description and first results⋆

Warwick E. Wilson,[1] R. H. Ferris,[1] P. Axtens,[1] A. Brown,[1] E. Davis,[1] G. Hampson,[1] M. Leach,[1] P. Roberts,[1] S. Saunders,[1] B. S. Koribalski,[1]† J. L. Caswell,[1] E. Lenc,[1] J. Stevens,[1] M. A. Voronkov,[1] M. H. Wieringa,[1] K. Brooks,[1] P. G. Edwards,[1] R. D. Ekers,[1] B. Emonts,[1] L. Hindson,[1,2] S. Johnston,[1] S. T. Maddison,[3] E. K. Mahony,[1,4] S. S. Malu,[5] M. Massardi,[6] M. Y. Mao,[1,7] D. McConnell,[1] R. P. Norris,[1] D. Schnitzeler,[1] R. Subrahmanyan,[5] J. S. Urquhart,[1] M. A. Thompson[2] and R. M. Wark[1]

[1]*CSIRO Astronomy & Space Science, Australia Telescope National Facility, PO Box 76, Epping, NSW 1710, Australia*
[2]*Centre of Astrophysics Research, University of Hertfordshire, College Lane, Hatfield AL10 9AB*
[3]*Centre of Astrophysics & Supercomputing, Swinburne University of Technology, Hawthorn, VIC 3122, Australia*
[4]*Sydney Institute for Astronomy, School of Physics, University of Sydney, NSW 2006, Australia*
[5]*Raman Research Institute, Sadashivanagar, Bangalore 560080, India*
[6]*INAF, Osservatorio Astronomico di Padova, Vicolo dell'Osservatorio 5, I-35122 Padova, Italy*
[7]*School of Mathematics and Physics, University of Tasmania, Private Bag 37, Hobart 7001, Australia*

Accepted 2011 May 10. Received 2011 May 9; in original form 2011 February 7

ABSTRACT

Here, we describe the Compact Array Broad-band Backend (CABB) and present first results obtained with the upgraded Australia Telescope Compact Array (ATCA). The 16-fold increase in observing bandwidth, from 2 × 128 to 2 × 2048 MHz, high-bit sampling and the addition of 16 *zoom* windows (each divided into further 2048 channels) provide major improvements for all ATCA observations. The benefits of the new system are: (1) hugely increased radio continuum and polarization sensitivity as well as image fidelity; (2) substantially improved capability to search for and map emission and absorption lines over large velocity ranges; (3) simultaneous multi-line and continuum observations; (4) increased sensitivity, survey speed and dynamic range due to high-bit sampling and (5) high-velocity resolution, while maintaining full polarization output. The new CABB system encourages all observers to make use of both spectral line and continuum data to achieve their full potential.

Given the dramatic increase of the ATCA capabilities in all bands (ranging from 1.1 to 105 GHz) CABB enables scientific projects that were not feasible before the upgrade, such as simultaneous observations of multiple spectral lines, on-the-fly mapping, fast follow-up of radio transients (e.g. the radio afterglow of new supernovae) and maser observation at high-velocity resolution and full polarization. The first science results presented here include wide-band spectra, high dynamic-range images and polarization measurements, highlighting the increased capability and discovery potential of the ATCA.

Key words: instrumentation: interferometers – methods: observational – ISM: general – galaxies: general – radio continuum: general – radio lines: general.

1 INTRODUCTION

The Australia Telescope National Facility (ATNF) provides open access to a large range of radio telescopes: the 64-m Parkes telescope, the Australia Telescope Compact Array (ATCA), the 22-m Mopra telescope and the Long Baseline Array (LBA) (see Frater, Brooks & Whiteoak 1992). Furthermore, the 'Australian SKA Pathfinder' (ASKAP), consisting of 36 × 12 m dishes, is currently under

⋆The Australia Telescope Compact Array is part of the Australia Telescope National Facility which is funded by the Commonwealth of Australia for operation as a National Facility managed by CSIRO.
†E-mail: Baerbel.Koribalski@csiro.au

Figure 1. The ATCA, located at the Paul Wild Observatory near Narrabri, some 550 km north-west of Sydney. Displayed are five of the six 22-m Cassegrain antennas, here arranged in one of the hybrid configurations which include two antennas on the north–south spur. The latter was opened on 1998 November 26, just over 10 years after the ATCA opening on 1988 September 2.

construction in Boolardy, Western Australia. With its expected 30 deg^2 field of view at 1.4 GHz, provided by novel phased array feeds, ASKAP will be a fast 21-cm survey machine, designed to carry out large-scale H I spectral line, transients and radio continuum surveys of the sky (Johnston et al. 2007, 2008).

In this paper we focus on the ATCA and its recent upgrade in bandwidth from 2×128 to 2×2048 MHz. While greatly increasing the sensitivity of continuum and spectral line observations (a factor of 16 in bandwidth gives a factor of 4 in continuum sensitivity) or, alternately, reducing the required observing time for a given continuum sensitivity by a factor of 16, this upgrade also enables simultaneous (full Stokes) multi-line observations, on-the-fly (OTF) mapping, as well as searching for emission and absorption lines over large velocity ranges. The high-bit sampling further improves sensitivity, mapping speed and dynamic range for radio frequency interference (RFI) suppression.

1.1 The Australia Telescope Compact Array

The ATCA is a radio interferometer consisting of six 22-m dishes (Frater & Brooks 1992), creating 15 baselines in a single configuration. While five antennas (CA01 to CA05) are movable along a 3-km long east–west track and a 214-m long north–south spur (see Figs 1 and 2), allowing the creation of hybrid arrays,[1] one antenna (CA06) is fixed at a distance of 3-km from the western end of the track. Each antenna currently has a set of six cryogenically cooled low noise receivers sampling the frequency range from 1.1 to 105 GHz (i.e. wavelengths from 3 mm to 30 cm), apart from CA06 which does not have a 3-mm receiver system (see Table 1).

[1] The ATCA hybrid configurations (H75, H168, H214) provide excellent *uv*-coverage over a 6-h integration time, thereby avoiding the need to observe astronomical sources at low elevations (highly beneficial for mm-wave observations where the Earth atmosphere adds substantially to the system temperature and consequently the rms noise).

Figure 2. The ATCA. Displayed are several antennas on the east–west track pointing at a source near the horizon.

A comprehensive description of the aperture synthesis and radio interferometry techniques is given in the expert lectures at the regularly held Radio Synthesis Schools (e.g. Perley, Schwab & Bridle 1988; Taylor, Carilli & Perley 1998) and also Thompson, Moran & Swenson (2002).

In their overview of the Australia Telescope, Frater et al. (1992) stated the aim to operate the array in 10 frequency bands, from 0.3 to 116 GHz. Initially, four bands (1.5, 2.3, 5.0 and 8.6 GHz) were available (James 1992; Sinclair et al. 1992) delivering excellent science (Ekers & Whiteoak 1992). The first stage of the millimetre-wave upgrade (Hall et al. 1997; Koribalski 1997; Brooks et al. 2000) added receivers at 15–25 GHz (15 mm), 30–50 GHz (7 mm) and 85–105 GHz (3 mm) [for details see Gough et al. (2004) and Moorey et al. (2008)]. A further extension of the highest frequency band to 77–117 GHz (as already available on the 22-m Mopra antenna; Moorey et al. 2006) is desirable in the future. In 2010 the 1.5 GHz

Table 1. Some ATCA properties [see the *ATCA Users Guide (Table 1.1)* for more details and up-to-date information].

ATCA observing bands	16 cm[a] (L/S)	6 cm (C)	3 cm (X)	15 mm (K)	7 mm (Q)	3 mm (W)
Frequency range (GHz)	1.1–3.1	4.4–6.7	7.5–10.5	15–25	30–50	85–105
Number of antennas	6	6	6	6	6	5
Number of baselines	15	15	15	15	15	10
Primary beam FWHM	44–16 arcmin	10.7–7.4 arcmin	6.3–5.1 arcmin	∼2 arcmin	∼70 arcsec	∼30 arcsec

Notes. ATCA observing information can be found at www.narrabri.atnf.csiro.au/observing, including a link to the CABB Sensitivity Calculator which is highly recommended to obtain observing characteristics (e.g. $T_{\rm sys}$) at specific frequencies and correlator settings (see also Fig. 3). The ATCA primary beam size (in arcmin) can be approximated by $50/\nu$ where ν is the observing frequency in GHz; the MIRIAD task PBPLOT provides details of the primary beam model (see Fig. 4).

[a] In 2010, the 1.5 GHz (20 cm) and 2.3 GHz (13 cm) bands were combined into one broad-band covering the frequency range from 1.1 to 3.1 GHz (now referred to as the 16-cm band).

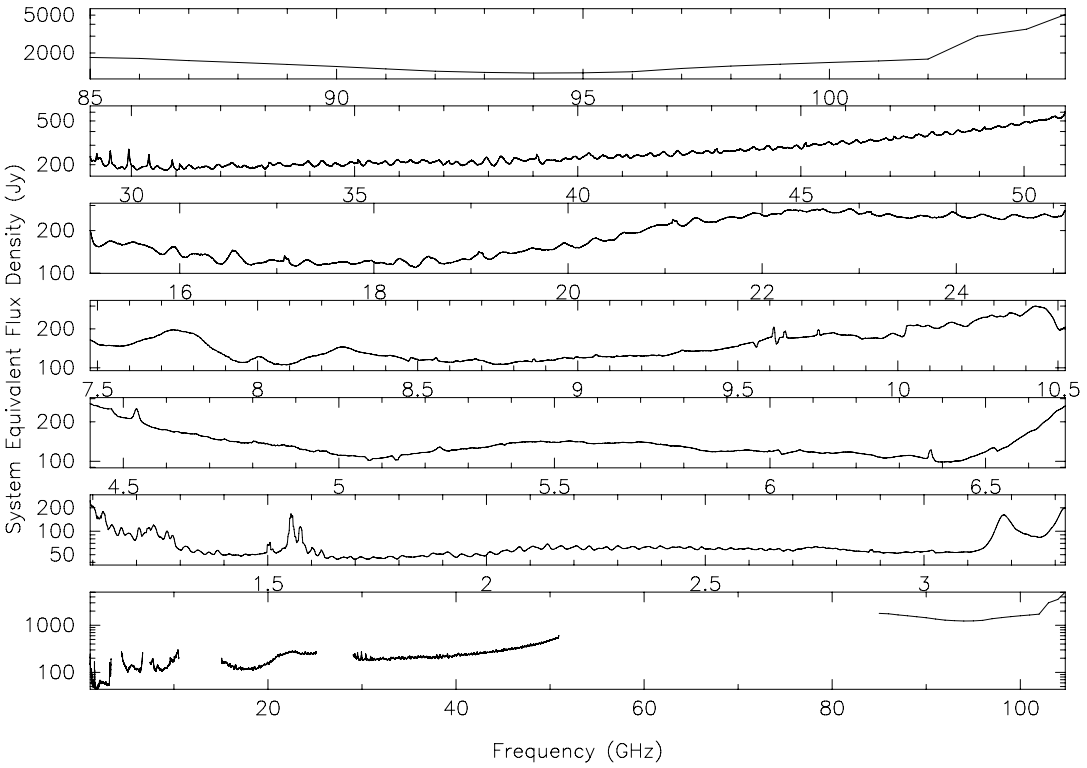

Figure 3. ATCA system equivalent flux density (in Jy, log scale), for each observing band, obtained at high elevation and under reasonable observing conditions. The measurements at frequencies from 1.1 to 50 GHz were made by Jamie Stevens in 2010 July/August using the CABB system, while the 3-mm measurements (80 to 105 GHz) were made by Tony Wong in 2004 September. The values are based on hot–cold load measurements and include the atmosphere at the time of the observation.

(20 cm) and 2.3 GHz (13 cm) bands were combined into one broad-band covering the frequency range from 1.1 to 3.1 GHz (effectively 10–30 cm; now referred to as the 16-cm band). See Table 1 for a summary of some basic ATCA properties. Because the ATCA system temperature and primary beam full width at half-maximum (FWHM) vary significantly across the available frequency range, these are shown in Figs 3 and 4.

In this paper, we describe the design and construction of the Compact Array Broad-band Backend (CABB), the first observational results and the scientific potential of the upgraded instrument. The sections are as follows: (2) CABB overview, (3) CABB design, (4) CABB installation and operations, (5) CABB data reduction software and (6) first CABB results.

The design and construction of other correlators for radio interferometers such as the Expanded Very Large Array (EVLA) and ASKAP are described in the respective overview papers by Perley et al. (2009) and DeBoer et al. (2009). SKA correlator advances are discussed by Bunton (2004) and software correlators by Deller et al. (2011).

2 CABB OVERVIEW

The CABB upgrade, described here, has provided a new wide-bandwidth correlator for the ATCA, which is significantly more versatile and powerful than the original correlator (Wilson et al. 1992).

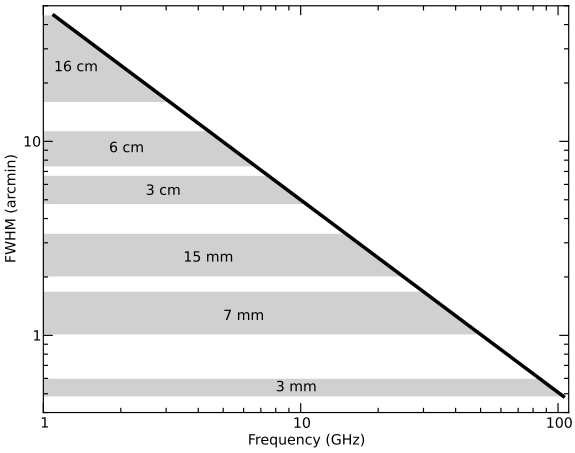

Figure 4. ATCA primary beam FWHM as a function of frequency; values were computed with the MIRIAD task PBPLOT. The currently available frequency coverage across all ATCA bands from 1.1 to 105 GHz range is indicated by the grey-shaded bands (see also the linear display of the ATCA frequency coverage in Fig. 3).

Table 2. Basic CABB configurations.

Configuration	Channel width	
	Primary band (MHz)	Secondary band (kHz)
CFB 1M–0.5k	1.0	0.488
CFB 4M–2k	4.0	1.953
CFB 16M–8k	16.0	7.812
CFB 64M–32k	64.0	31.250

The maximum bandwidth of the ATCA has been increased from 128 MHz to 2 GHz (dual polarization) in each of two independently tunable intermediate frequency (IF) bands, while CABB also increased the velocity resolution and delivers full Stokes parameters in all observing modes. Furthermore, the digitization level has improved from 2 bits to 9 bits, increasing correlator efficiency and consequently lowering $T_{\rm sys}$. In the following we list the advances provided by the new system.

(i) The correlator is supplied with an 8 GHz wide IF band from the front-end. Within this, the observer can tune (within the receiver limits; see Table 1) two independent 2048 MHz windows (dual polarization) for correlation. This represents a factor of at least 16 increase in the useable bandwidth over the original ATCA correlator. Each 2 GHz window can be split into 2048, 512, 128 or 32 primary channels (see Table 2).

(ii) Up to 16 high-velocity resolution *zoom* windows can be placed anywhere within each 2048 MHz band. Each *zoom* window covers the width of one 'continuum channel' in the primary band and further splits it into 2048 high-resolution spectral channels (as illustrated in Fig. 9). Basic correlator configurations are listed in Table 2.

(iii) CABB combines high spectral resolution with full Stokes imaging, e.g. needed for the study of Zeeman splitting in masers. All Stokes parameters are computed by the new correlator in all available modes. The original ATCA correlator was unable to provide cross-polarization correlations when used in modes with high spectral resolution.

(iv) Sampling resolution and digitization accuracy have increased from 2 bits with the original correlator (Wilson et al. 1992) to 9 bits with CABB (see Section 3.2), increasing the correlator efficiency from <0.88 to ≈ 1 (i.e. reducing the ATCA $T_{\rm sys}$ by $\sim$14 per cent), the dynamic range and tolerance to RFI.

(v) Internally, CABB constructs a polyphase filter bank, providing spectral channels that are largely independent with $\approx$80 dB isolation from adjacent channels. This avoids the ringing that was commonly seen with the original ATCA and other correlators while observing narrow spectral lines.

(vi) Modes providing high-velocity resolution (for spectral line studies), high time resolution (for the study of fast transients) or pulsar binning come as an addition to the basic wide-bandwidth modes.

(vii) CABB also provides auto-correlation data.

These improvements have a major impact on the scientific ability of the ATCA (see examples in Section 6), including the following.

(i) The much larger bandwidth reduces the time required to reach any particular continuum sensitivity, and the increased sampling depth allows for higher dynamic range and lower $T_{\rm sys}$.

(ii) Narrow, independent channels allow for precise excision of narrow-band interference.

(iii) The division of the primary IF bands into a large number of channels substantially improves the *uv*-coverage for any single observation when multi-frequency synthesis (MFS) is used (see Section 5.4).

(iv) At low frequencies (1–10 GHz), CABB's large fractional bandwidth makes it possible to study the spectral behaviour of continuum sources without resorting to frequency switching (see Section 6.7).

(v) At high frequencies (16–105 GHz), CABB's large frequency coverage allows projects to simultaneously observe multiple spectral lines that fall within 8 GHz of each other; it also provides broad velocity coverage to carry out reliable searches for molecular lines at high redshifts (see Section 6.9).

(vi) The CABB *zoom* modes enable simultaneous observations of multiple spectral lines at high-velocity resolution (see Section 6.3).

(vii) The CABB *zoom* channels can also be concatenated to provide a wide velocity range, while maintaining high velocities resolution (see Section 6.5).

(viii) The correlator can be configured to provide the most suitable compromise of sensitivity, speed and resolution for any particular observation. This is achieved by varying the width of each channel in the primary bands (see Table 2).

3 CABB SYSTEM DESIGN

The two main objectives of the ATCA broad-band upgrade were to increase the sensitivity and versatility of the instrument while providing a test bed for technologies which were judged to be important in the development of the Square Kilometre Array (SKA). The improvement in sensitivity was achieved by increasing the maximum available bandwidth from 128 MHz to 2.048 GHz. A *Field Programmable Gate Array* (FPGA) based correlator gave the required versatility, with its capability of being configured into many different operating modes. An important goal was to improve the spectral line capability of the instrument, particularly at the higher observing frequencies. Technologies employed, such as multi-bit digitizing, high bandwidth digital data transfer over fibre optic cables and advanced signal processing were all considered to be applicable to the SKA.

The first stage of the CABB backend selects two independently tuneable 2 GHz bands from the active receivers. Two orthogonal linear polarizations are available from each band. The four resulting

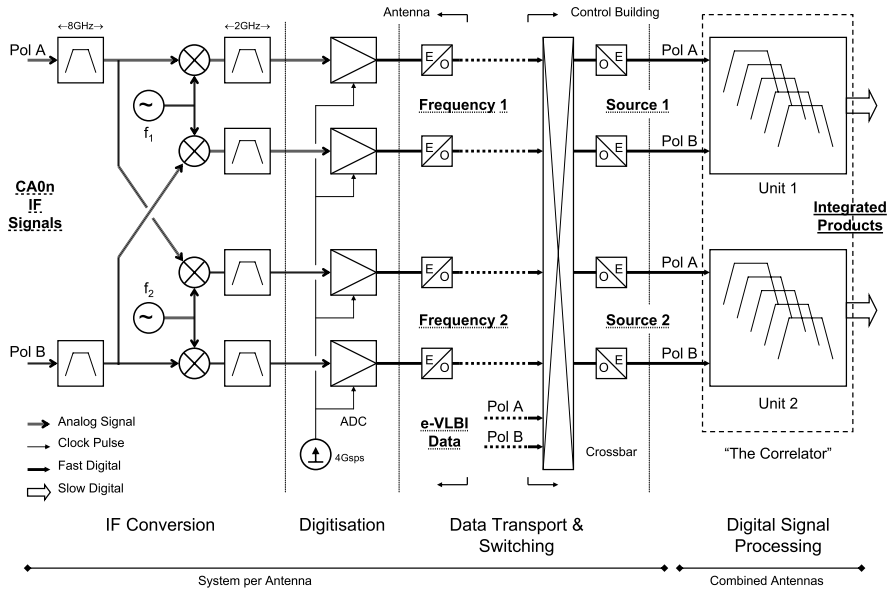

Figure 5. CABB system overview.

2 GHz wide IF bands are digitized and sent over fibre optic cables to the central control building. Here, they enter the correlator, where the online signal processing takes place. A block diagram of the system is shown in Fig. 5, and details of the signal path and the processing are described in the following sections.

Associated analogue-to-digital conversion (ADC) requirements are pushing the limits of high-speed sampling and quantization techniques. 9-bit data samples and 17-bit (minimum) internal signal paths through to the integrators provide performance approaching analogue correlation but with the obvious advantages of digital processing. Combined with excellent channel selectivity the system is significantly more robust against strong interference than 2-bit correlators (Ferris & Wilson 2002).

These new technologies are direct candidates for signal processing on the proposed SKA and its precursors, such as the ASKAP. CABB includes a total of eight antenna ports, allowing two antennas to be added to the existing six antennas of the ATCA, providing both a more powerful instrument and a mature test bed for the SKA pathfinders.

In the following we describe the IF conversion system (Section 3.1), the digitizers and data transmitters (Section 3.2), data transport and reception (Section 3.3), the digital filter bank correlator (Section 3.4), the signal processing (Section 3.5), the correlator hardware implementation (Section 3.6), the rear transmission module (Section 3.7), the front board (Section 3.8) and the control software (Section 3.9). In Section 3.10 we briefly look at the role of CABB in demonstrating novel technologies for SKA. The last section (Section 3.11) gives an overview of the CABB installation.

3.1 IF conversion system

The modular CABB IF conversion system resides in a shielded rack at the vertex of each antenna of the ATCA. The functionality of this system (see Fig. 6) includes primary band filtering 4.2 to 12 GHz, stepped level control of 16 dB, sub-band selection for image management and frequency translation to suit the digitizer requirement. The definition of the IF band is achieved by anti-aliasing filters covering 2.048 to 4.096 GHz, corresponding to the second Nyquist zone of the ADC.

The signal flow in Fig. 6 indicates the fundamental elements, which were selected with a significant emphasis on low cost where possible and the reuse of ATNF designed assemblies. Each input pair (two polarizations) is passively split allowing for two discretely tuneable 2 GHz wide slices of the incoming primary signals. The assembly is physically divided into three sections, the radio frequency (RF) module, the conversion module and the IF module, briefly described below.

(i) Primary band filtering, loss slope equalization and passive power splitting are achieved in the *RF module*.

(ii) Slope compensated low noise amplification, digitally controlled step attenuation, image suppressing sub-band selection and frequency translation are achieved in the signal processing part of the *conversion module*. Support for maintenance is provided by low-level monitoring outputs. Suppression of potential local oscillator (LO) leakage contamination from the split frequency design is provided by both fixed and tracking filtering. The provision of a yttrium iron garnet (YIG) tracking LO rejection filter is only made tractable by the integrated tuning management incorporated into the optically slaved LO system (see below).

(iii) The *IF module* provides slope-compensated amplification, low-level monitoring outputs and anti-aliasing band filtering.

In an effort to minimize the impact on system stability when moving to the increased fractional bandwidth required by CABB, a newly conceived and designed group of filters following a castellated wall ridged waveguide topology (Bowen et al. 2010) were used. These filters have low insertion loss, low sensitivity to temperature change and high component repeatability. They are used in the primary input filtering, LO noise filtering and the IF anti-aliasing filter.

Two central site reference frequencies, each in the range of 8 to 14 GHz, are transmitted to each antenna via separate intensity modulated optical fibre links. The antenna YIG oscillators are then offset phase locked to the optical references. The specific choice in YIG oscillators for the frequency conversion was heavily biased

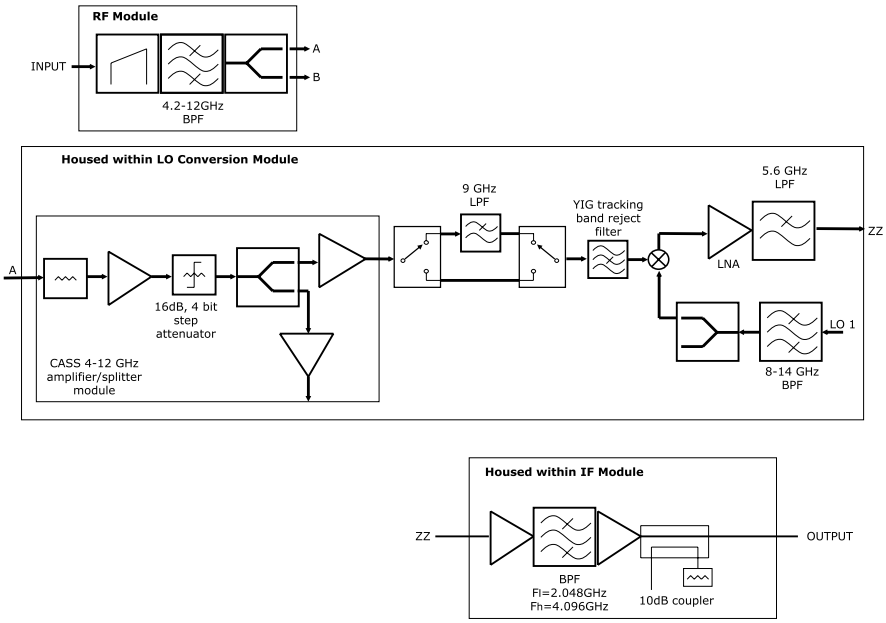

Figure 6. The three sections of the CABB conversion system: (1) RF module, (2) conversion module and (3) IF module. BPF = bandpass filter, LPF = lowpass filter and LNA = low noise amplifier.

towards oscillators having low in-band phase noise and very low broad-band noise in order to limit the coherent noise contamination seen at the IF.

The system's dynamic range suffers as a result of the need to place a hard bound on the IF module's saturated output power level to prevent degradation or destruction of the digitizers. The original low-end specification of the primary band was modified from 4 to 4.2 GHz due to excessive direct leakage into the output band. Triple balanced mixers were chosen due to their enhanced leakage suppression and lower spur product generation to further reduce spurious signal generation.

3.2 Digitizers and optical data transmission

A major innovation required to realize the CABB specifications was the development of an ADC/data transmitter module (see Figs 7 and 8) capable of supporting the 4.096 gigasamples s^{-1} (GS s^{-1}) rate required for processing the 2.048 GHz of bandwidth demanded by the upgrade. The project ambitiously aimed to implement quantizing at bit levels significantly higher than those traditionally undertaken in radio astronomy correlators. Typically, 2-bit sampling has been used. The major goal was to allow for faithful handling and removal of RFI in the signal processing as well as increased sensitivity. There were no commercially available ADC devices that met these specifications at the time the design commenced.

The need for high dynamic range, mostly due to RFI (but also required for deep fields or in the vicinity of extremely strong radio sources), makes it necessary to use sampling at high bit levels. In the noise-dominated case (i.e. classical astronomical observation), the loss due to 2-bit (4-level) quantization is large (van Vleck & Middleton 1966; Cooper 1970), leading to a significant (>14 per cent) increase in the system temperature, $T_{\rm sys}$. A high-resolution digitizer with sufficient bits can be operated with negligible increase of $T_{\rm sys}$, i.e. the correlator efficiency is ≈1.

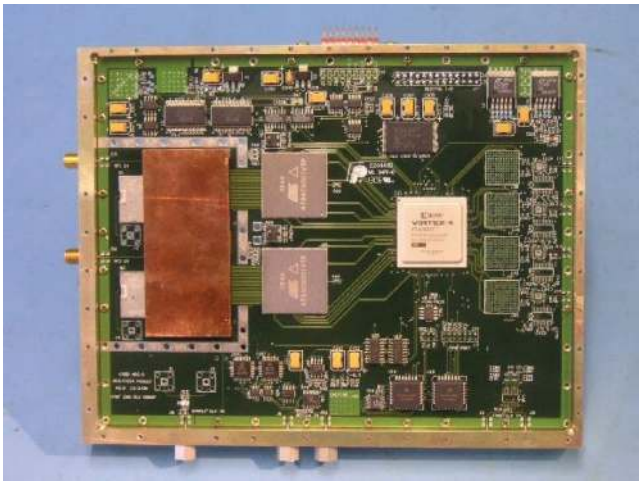

Figure 7. The CABB ADC/data transmitter module (see Section 3.2).

Figure 8. The CABB DSP board.

The solution was to develop an ADC subsystem composed of two commercial 2 GS s^{-1} 10-bit ADC chips operated in an interleaved fashion. The same input is distributed to the two converters with their sampling times in precise anti-phase, to give an equivalent 4.096 GS s^{-1} 10-bit converter. This requires extremely tight matching of the two channels in terms of sampling phase, gain, bandwidth and DC offset. High-resolution calibration and trimming circuitry that can control these parameters to the level required have been incorporated on the board, and algorithms developed to automatically measure, and adjust, these trims in real time. Experience has shown that the system stability is such that only a single calibration is required. The board and ancillary systems are housed in a module that is located in each antenna's shielded rack.

Performance achieved over the 2.048 to 4.096 GHz CABB IF band at a full sampling rate is a signal-to-noise ratio of typically 38 dB, equivalent to approximately six effective digitizer bits, and spurious free dynamic range of 39 dB.

In addition to ADC the CABB ADC/Data Transmitter module performs framing and transmission of the ADC data. It takes 40 gigabits s^{-1} (gbit s^{-1}) of data from the digitizer and frames it into four 10 gbit s^{-1} serial data streams which are passed to laser driver chips driving externally modulated lasers at four different optical wavelengths. These are wavelength division multiplexed on to a single fibre for transport from the antenna to the central control building. Of the 10 bits of sampled data, 9 bits are transported over the link. The remaining link overhead is used for implementing a custom synchronization and timing protocol that enables each of the 10 gbit s^{-1} data streams to be re-aligned and allows precise tracking of the delays on each path back to the control building.

The digitizer/transmitter module has been designed to be as general as possible to allow it to be used in other applications apart from the CABB upgrade. It has, for example, been used as two independent 1 GHz bandwidth ADCs in the ATNF Pulsar Digital Filterbank systems at the Parkes 64-m telescope (Manchester et al. 2010), for radio transient detection experiments[2] with both Parkes and the ATCA and as an RFI transient detector at the ASKAP Boolardy site.

3.3 Data transport and reception

The digitized data are transported to the correlator in the central control building via a single optical fibre feed from each digitizer. Each optical fibre carries four 'colours' at the 200 GHz ITU frequencies of 193.8 THz, 193.6 THz, 193.4 THz and 193.2 THz. Each laser is co-packaged with an electro-absorption modulator and is intensity modulated at 10 gbit s^{-1}.

In the central control building, the four colours on each fibre are de-multiplexed and each optical signal is then detected by a Receive Optical Sub-Assembly (ROSA) which incorporates a PIN detector and a transimpedance amplifier. The electrical outputs to the correlator are Current Mode Logic differential signals. The ROSAs are part of the Rear Transition Module (RTM), which forms the interface between the fibre transmission and the correlator. The RTM is described in more detail below.

3.4 The digital filter bank correlator

The central feature of CABB is the FX-type spectroscopic correlator. Its design supports primary channelization with 1, 4, 16 and 64 MHz resolution consistent with science requirements across the ATCA input frequency range of 1.1 to 105 GHz. For each frequency channel on each baseline the four cross-products of the two polarizations are formed. Also, for each frequency channel and for each antenna the two polarization auto-correlations and the cross-polarization product are formed, including a facility for synchronous extraction of a switched calibration signal. The latter is injected coherently into the orthogonal linear polarized receivers for polarization calibration. All products are always available across the full 2.048 GHz signal bandwidth.

At the same time up to 16 *zoom* windows (channels) at the primary resolution bandwidth, but half its channel spacing, may be selected for secondary processing into 2048 channels each. Again, all four polarization products are recorded. The available configurations are shown in Table 2. When two or more adjacent *zoom* windows are chosen, they are aggregated to provide a seamless high-resolution spectrum across their net bandwidth. Passband ripple from the primary filter bank is automatically removed. This system provides for the simultaneous observation of multiple widely spaced spectral lines, plus the underlying continuum. An example of a *zoom* band setup is shown in Fig. 9.

Antenna signals with the primary channelization may also be formed into beams for very long baseline interferometry (VLBI), pulsars, spacecraft tracking, etc., with the native linear polarizations added in quadrature to provide circular polarizations as required.

There are two such correlator units, one for each of the ATCA's independently tuneable observing frequencies. Where the front-end bandwidth allows, observations at full specifications across a total of 4 GHz are possible. Alternatively the units may be tuned to the same input frequency to repeat the observation with a different set of correlator configuration parameters.

3.5 Signal processing

The essential structure of the correlator signal path is shown in Figs 10 and 11. Beginning with high-resolution IF data from the ADCs, the bulk of the geometric delay is removed to the nearest sample time in the 'Coarse Delay' units. The 2 GHz wide signals are then analysed into many baseband channels as per Table 2 in the primary polyphase digital filter banks (PDFBs). The flat-topped, sharp cut-off, deep (~ -80 dB) stopband filter shape achieved (see Fig. 12) far exceeds the requirements of good measurement. Its purpose is to prevent the spread of strong RFI from channel to channel. The filter banks output only the positive frequency signal components to make subsequent processing easier.

Fringe rates are stopped on a per channel basis. Since the channel bandwidths are much smaller than their centre frequency in the sky, the timing residuals left by the 'Coarse Delay' are manifest as all but constant phase shifts. This is accurately removed by adding an offset, 'Fine Delay', to the fringe phase. An additional $\pi/2$ can be added to the B polarization phase whenever necessary to generate circularly polarized beams in the beam formers.

After the 'Fringe Rotators' the signals are wavefront-aligned at all frequencies across all antennas. At this point (see Fig. 10) the

[2] During the CABB development phase (before 2009 March), three antennas of the ATCA were used to hunt for ultra-high energy (UHE) neutrinos using the lunar Cherenkov technique. For details of the LUNASKA experiments see James et al. (2010, 2011) and McFadden et al. (2008). By-passing the original ATCA IF system, the teams obtained 600 MHz of bandwidth in the then available 20-cm band (1.2 to 1.8 GHz). Each polarized data stream was fed through an analogue de-dispersion filter (Roberts & Town 1995) before being sampled by the CABB ADC board at 2 GS s^{-1} with 8-bit effective precision.

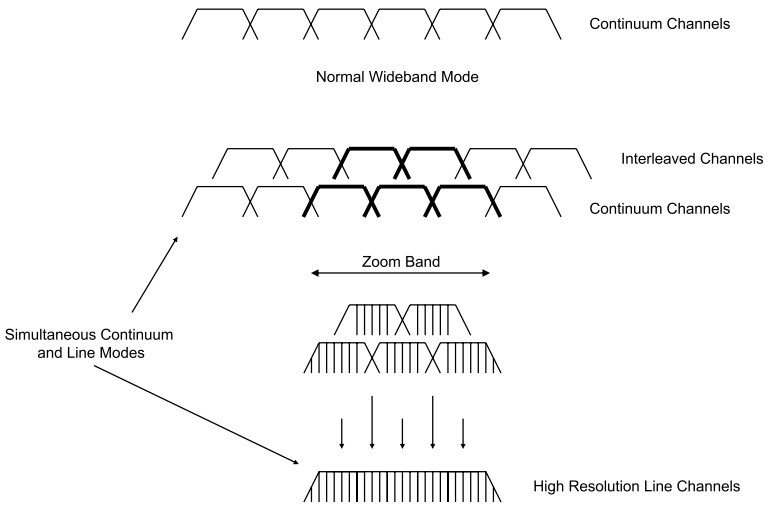

Figure 9. CABB provides up to 16 *zoom* windows which can be allocated individually or in groups. Here, we show an example where five *zoom* windows are concatenated (overlapped in steps of 0.5 channels) to increase frequency coverage while maintaining high-velocity resolution and high dynamic range.

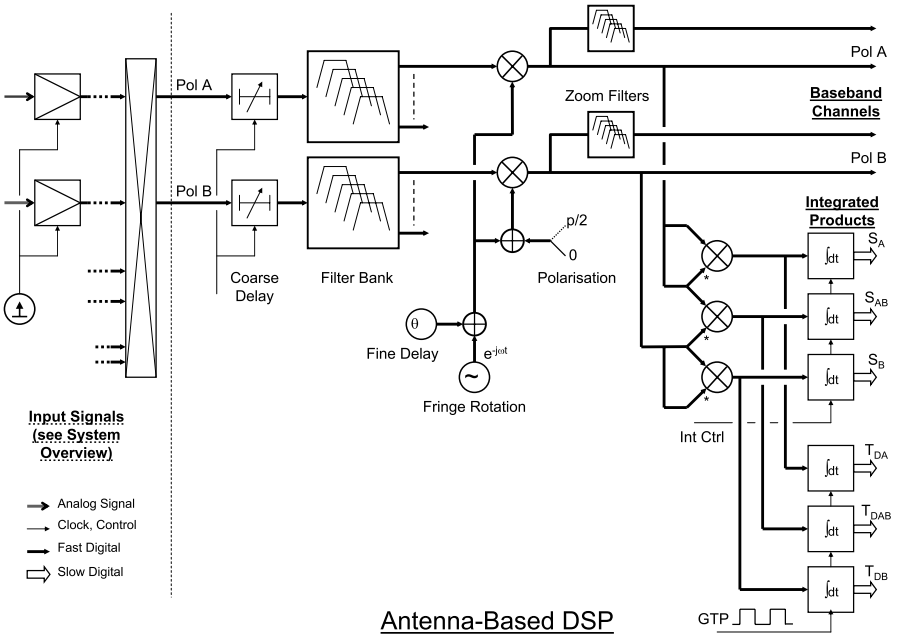

Figure 10. CABB signals from orthogonal linear polarizations are digitized, channelized, fringe-stopped and calibrated.

user-selected subset of primary channels is fed to narrow-band PDFBs to produce the high-resolution *zoom* channels. The antenna auto-correlations and X/Y phases[3] are also formed, using synchronous integration to extract the signature of the low-level switched noise diode calibration signal which is injected into the receiver horn. These signals are used to monitor and refine system calibration.

Baseband channels from all antennas are brought together in the 'Correlation Cell Array' (see Fig. 11). In each cell the signals from one antenna are multiplied by the conjugate of the corresponding signals from another antenna, and the products integrated in simple accumulators. All four possible products are formed. Thus each cell computes the complex visibilities for one baseline. These are normally unloaded at 10-s intervals, but shorter integration times are supported (110 ms in pulsar binning mode and 20 ms in high time resolution). *Zoom* channel processing follows the same form and is synchronized with the primary channels so that all output data have the same epoch.

Signals from all antennas can be added to produce phased array beams, with the option of applying complex weights to steer the beam around within the primary antenna pattern. The resulting signals are available outside the correlator for processing in other equipment.

The digital signal path begins with 9-bit ADC data, and word size expands with natural growth plus the addition of guard bits. There is no clipping or re-quantization, and noise addition due to rounding and aliasing is carefully controlled. The dynamic range of the ADC is preserved so that expected variations in system temperature, front-end passband slope and ripple, and strong astronomical sources are accommodated without resort to gain control or

[3] Instrumental phase difference between X and Y polarization channels.

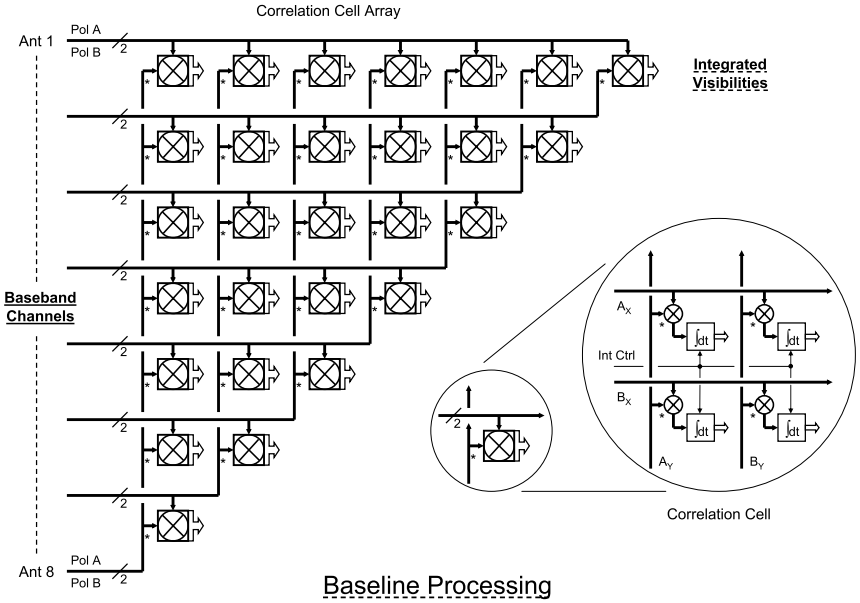

Figure 11. CABB polarization pairs from each antenna are multiplied with the conjugated pairs from every other antenna. All four cross-products are formed and integrated.

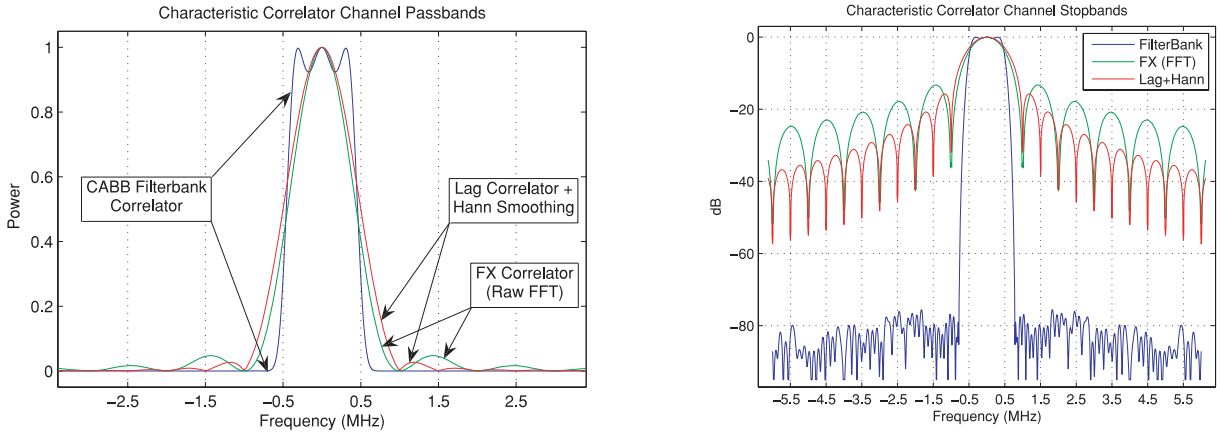

Figure 12. Comparison of the CABB Filterbank 1 MHz channel 'square' response (blue lines) with those of classic 'FX' correlators (green lines) and lag/'XF' correlators (red lines); the FX response function is $\mathrm{sinc}^2(\nu)$, while the lag response is $\mathrm{sinc}(\nu)$ where ν is the frequency. The absence of sidelobes in the CABB Filterbank channels is remarkable (for details see Section 4.2). Left: the three functions are plotted on a linear scale over ± 3.5 MHz and (right) on a log scale over ± 6 MHz.

non-linear correlation corrections, and there is still headroom to tolerate RFI without distortion or compression.

The combination of high dynamic range in the time domain and high selectivity in the filter bank (see Fig. 12) ensures robustness against RFI. This linear, stationary signal path will provide an ideal platform for future RFI removal instigations (Ekers & Bell 2001).

Contrary to tradition there is no 'Correlator Chip' ASIC in this design. Instead, all signal processing takes place in FPGAs wherein ready access to a very high density of logic resources allowed the development of an instrument with a level of sophistication unattainable in a hard-wired circuit. In addition, flexibility through reprogrammability has supported progressive development with evaluation on telescopes, multiple independent configurations (listed in Table 2), a shift from one generation of FPGAs to the next to take advantage of the latest technology and the spinoff of several related but distinct instruments. Separating the signal processing from the hardware also allowed the parallel and largely independent development of the latter, a significant engineering project in its own right. A by-product of this flexibility has been the complexity of modes which are possible, leading to an increase in time needed for testing and commissioning.

3.6 Correlator hardware implementation

The architecture of the hardware platform, as depicted in Fig. 13, is driven by the need to connect signal paths from the antenna-based processing to the baseline-based processing, the details of which have been described in the previous section. It is well known that for large interferometers this apparently mundane task (which grows as the square of the number of antennas) is the main obstacle and becomes the major cost driver. For the modestly sized CABB correlator the solution was to adopt the newly announced Advanced Telecom Compute Architecture (AdvTCA) chassis, a commercial item developed by and for the telecommunications industry. Its backplane includes a mesh network, providing a high bandwidth link from every slot to every other slot, exactly as required. Each of

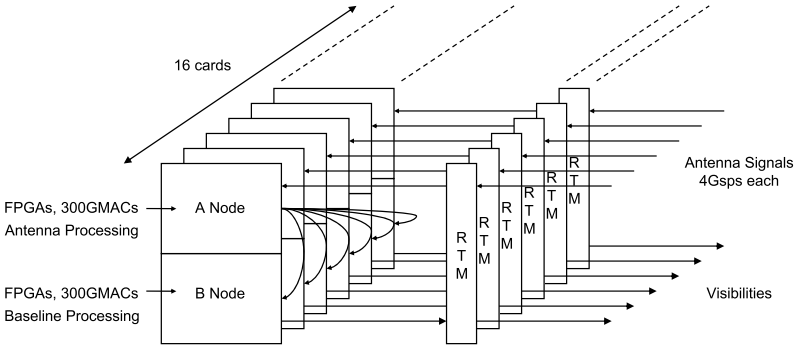

Figure 13. Schematic of the AdvTCA chassis (see Section 3.6). Every A node connects to every B node with four 2.5 Gbps links. The RTM provides the physical interfaces to the external environment.

16 card slots can accommodate a large 'Front Board' which connects to the mesh and supports the signal processing, and a smaller directly linked board, the RTM, which provides the physical interfaces to the external environment.

The CABB Front Board has half of its FPGA resources connected to the input side of the mesh, supporting most of the antenna-based digital signal processing (DSP; see Fig. 8). The remaining resources are driven by the output side of the mesh and support the baseline-based DSP, plus the antenna-based Integrated Products since they require both polarizations. Thus, each mesh input node sinks the full spectrum from 1/16 of the Frequency 1 (or 2) antenna IFs, and each mesh output node sources 1/16 of the spectrum from the full set of Frequency 1 (or 2) antenna IFs. In this way one AdvTCA chassis supports a correlator for eight antennas, the six ATCA dishes plus two further antennas, providing a mature test bed for the SKA pathfinders.

3.7 The rear transition module

The functions of the RTM are as follows.

(i) To receive the four optically transported 10 gbit s^{-1} data signals from one digitizer and to convert them back to electrical signals using one ROSA per 'colour' and then synchronize and merge these four separate data streams into one parallel data stream.

(ii) To receive and buffer the main system clock signals of 256 MHz, 128 MHz, 32 MHz and 160 MHz.

(iii) To receive and buffer supplementary control signals, including a one pulse per second timing reference signal.

(iv) To provide four, four-lane Infiniband channels, with each lane capable of up to 3.125 gbit s^{-1} data rate, for connection to or from external systems as required.

(v) To provide a mass storage device for the Front Board's embedded processor.

(vi) To provide two ethernet connections to the control and data networks.

Most of the logic functionality is achieved using one FPGA. This FPGA may be set to be configured from an onboard Programmable Read-Only Memory (PROM); however it is generally configured from the Front Board's embedded processor.

3.8 The front board

The complexity of the 'Front Board', also known as the CABB Signal Processing card, is indicated by its specifications. These include a 26-layer printed circuit board (PCB) measuring 322 × 280 × 3 mm standard AdvTCA form factor, 4188 components, and ≈20 000 nets and 230 000 holes. The major elements in the processing card are as follows.

(i) 10 signal processing FPGAs that have the following functions: (a) to perform coarse data delay functions and implement a filter bank; (b) to provide $4 \times 16 = 64$ high-speed 2.5 gbit s^{-1} communications channels, four to each of the other 15 cards and one loopback. Each communication channel is full duplex, meaning that there is an independent 10 gbit s^{-1} TX and 10 gbit s^{-1} RX data path to every processing card from every other card; (c) to implement a correlator and (d) provide for an external high-speed data interface for applications such as VLBI and spacecraft tracking.

(ii) A small control computer with a Geode LX800 processor and 128 megabytes (Mbytes) of memory and onboard 10/100 Mbit s^{-1} ethernet. The system communicates with the processing FPGAs via a standard PCI bus. An additional ethernet interface chip is installed on the processing card to enable 1 gbit s^{-1} ethernet communications.

(iii) Two control FPGAs, one distributing control and monitoring data to all signal processing FPGAs and the other distributing accurate timing signals to all FPGAs. Both interface directly to the above system over the local PCI interface bus.

(iv) Six mini dual in-line memory modules (DIMMs) of DDR2 RAM, each supporting up to 1 gigabyte (GByte). Each correlator FPGA is connected to two modules and the delay FPGA is connected to two modules.

(v) A flexible clock distribution network allowing either externally provided reference signals from the RTM or locally generated signals, to be distributed to all processing FPGAs. Each processing card contains four LOs operating at 66 MHz, 200 MHz, 266 MHz and 156.25 MHz. The clock distribution network can be configured to shutdown if a temperature sensor surpasses a preset threshold.

(vi) System health monitor points for all onboard-generated voltages, all FPGA temperatures and PCB temperatures around the board.

(vii) An isolated power conversion module with a 48 V input generating all the required voltages for the FPGAs onboard. A large distributed heat sink covers all signal processing FPGAs to distribute heat over the entire card and reduce hot spots. Each card is rated at 200 W.

All signal processing FPGAs are connected to each other with parallel low voltage differential signalling (LVDS) data busses of varying widths. All data pairs run at a common data rate of 512 Mbps. Data arrive from the rear IO card across the AdvTCA zone 3 connector and are received by the coarse delay FPGA. It is then transferred to the two filter bank FPGAs. These FPGAs are

interconnected allowing the signal processing required for the filter bank to be split across both. Each filter bank FPGA is connected to one of the data distribution FPGAs. Data are distributed between these four FPGAs as well as to and from every other processing card in the AdvTCA rack. Every data distribution FPGA has a dedicated link to each of the two correlator FPGAs, and each correlator FPGA has access to two modules of DDR memory for data accumulation.

3.9 Control software

Control of the CABB hardware and firmware has been integrated into the standard correlator control software package, which itself has been developed over many years to support backend systems at all ATNF observatories. The major new functions required for CABB were antenna hardware switching control, LO setting, correlator configuration control, delay tracking, procedures for the calibration of delay, phase and amplitude, system monitoring and data collection and archiving. The fact that much of the functionality of the previous backend system has been moved into the correlator required a significant expansion of the correlator control software. Examples of this are the delay tracking and narrow-band conversion systems, which were previously located in special purpose hardware in the antennas.

The delay tracking software uses the GSFC Mk-5 VLBI Analysis Software CALC (Gordon 2004). A custom interface to the CALC package has been created to facilitate its use in the real-time CABB application.

3.10 Square kilometre array development role

The construction of CABB (see Fig. 14) embodied the role of demonstrating enabling technologies for the SKA. Novel features include the digital filter bank correlator architecture, the high 2 GHz signal bandwidth and 4 GHz total bandwidth, high-resolution digitization followed by a linear, stationary, signal path, RFI robustness, and simultaneous continuum and spectral line observations at full specifications across the full bandwidth. The correlator provides extra ports to incorporate two additional external antennas. Wideband data produced by CABB provide challenging input to a new generation of off-line data reduction and imaging software tools under development for ASKAP and the SKA.

Figure 14. The CABB rack as installed in the fully shielded ATCA correlator room.

The Mopra wide-band system, the CABB 2 GHz correlator in Narrabri, the SKA Molonglo Prototype (SKAMP) correlator at Captain's Flat (Adams, Bunton & Kesteven 2004), the Murchison Widefield Array (MWA) correlator (Lonsdale et al. 2009) and the Parkes Testbed, where a 48 (upgradable to 192) input beamformer has been implemented, can be considered prototype systems for the design of the ASKAP correlator (DeBoer et al. 2009).

4 CABB INSTALLATION AND OPERATIONS

The installation of CABB required a significant shutdown of the Compact Array totalling 6 weeks in 2009 March/April. The task was lessened somewhat through progressive installation over the year prior to the major installation of an interim CABB system. The interim system, which ultimately provided a single 2 GHz bandwidth, with dual polarizations for five of the six ATCA antennas, was able to be operated in parallel with the original correlator system, allowing valuable comparisons and cross-checks to be made. In concert with the signal transmission and processing hardware changes, modules to interface the current suite of receivers to the new system have been fabricated and installed. CABB operations and scientific commissioning were interleaved with engineering maintenance periods in late 2009 April. The new CABB system has also required significant changes to the array control and monitoring software, which has taken place in parallel with the hardware changes. In addition, the ATCA data analysis package MIRIAD has required revision and extensions to enable significantly larger CABB data files to be processed.

The first mode available for general observing consisted of 2×2048 MHz bandwidths with 2048 channels across each band, corresponding to a 1 MHz spectral resolution. For VLBI and NASA tracking a single 64-MHz channel observing mode was also made available. Table 2 summarizes the basic modes; currently available are as follows.

(i) CFB 1M–0.5k: a bandwidth of 2 GHz divided into 2048×1 MHz channels and (optionally) a fine resolution of 0.5 kHz in up to four *zoom* bands in each of the two IF bands have been available since 2010 May. The first observations with 16×1 MHz *zoom* bands were obtained on 2010 December 17 (see Fig. 26 later).

(ii) CFB 64M–32k: a bandwidth of 2 GHz divided into 32×64 MHz channels and (optionally) a fine resolution of 32 kHz in up to four *zoom* bands in each of the two IF bands. Since 2010 October a single 64 MHz channel (divided into 2048 sub-channels) is available in each IF. We hope that all 32 channels and *zoom* channels will be available later in 2011.

(iii) *Pulsar binning modes* were successfully tested in 2010 December (see Section 6.13). The minimum time bin is $\sim$110 μs, allowing, for example, 32 phase bins across the period of a 3.5 ms pulsar.

(iv) *High time resolution modes* ($\sim$10 ms) were implemented in 2011 January, with 4 MHz frequency resolution across each of the two 2-GHz IF bands.

4.1 CABB milestones

The CABB project commenced in 2002 January and had at its core a new DSP system based on a novel PDFB structure developed at ATNF. Key milestones on the path to completion of CABB included

provision of the Mopra Spectrometer (MOPS;[4] see e.g. Walsh et al. 2010; Urquhart et al. 2010; Muller et al. 2010) in 2006, delivering 8 GHz of bandwidth, and the Pulsar Digital Filterbanks for the 64-m Parkes dish (Ferris & Saunders 2004).

CABB replaces the Compact Array's original signal processing and digital correlator system (Wilson et al. 1992). Those systems, at the time of their design and construction in the 1980s, were 'state-of-the-art' and gave the ATCA a competitive edge when it began operating in 1990 (Frater & Brooks 1992).

First fringes with the interim CABB system were obtained on 2008 May 23 between CA02 and CA03. On 2008 August 12, a three-baseline system was first demonstrated with the addition of CA05, with fringes obtained on a single polarization with a 128 MHz bandwidth, enabling further testing to be carried out. In early 2008 November, full 2 GHz auto-correlation spectra were being obtained from CA01 to CA05, followed by the first CABB image (single IF, 128 MHz bandwidth, full polarization) in early December. Comparison with data from the original (pre-CABB) correlator indicated the CABB system was working well. In late 2008 December and early 2009 January, the CABB bandwidth was gradually increased towards the full 2 GHz, with additional imaging observations being made to test the flow of data from the correlator and through MIRIAD. In 2009 February, the first observations utilizing the full 2048 channels were made with the interim CABB system (five antennas, single IF). On February 23, CA06 was taken off-line and preparations started for the full CABB installation. A 6-week shutdown ran from 2009 March 2 to April 14, followed by a week of scientific commissioning (in the H168 array). Scheduled observing started on 2009 April 22.

The CABB shutdown diary, available online, provides a lively documentation of the progress during that period. CABB fringes were progressively obtained by the Compact Array antennas, with first CABB fringes to all six antennas obtained on 2009 April 1. Upgrades to the ATCA operations and monitoring software and to the popular MIRIAD data reduction package were carried out in parallel (see Section 5).

First scientific results, obtained by operations and astrophysics staff as well as ATNF co-supervised students, were presented during the CABB Science Day on 2009 May 13 (available online). Initially, only bands from 3 mm to 6 cm (see Fig. 15) were available for testing, with poor weather conditions severely limiting observations in the 3-, 7- and 12-mm bands. The 13- and 20-cm bands (now replaced by a combined and much broadened 16-cm band) were available for testing from 2009 May 15. The large number of 'dead channels' (due to missing CABB boards in 2009 April and May) made it difficult to obtain presentable, wide-band spectra.

The first CABB zoom mode observations with a single ATCA baseline were taken in 2010 March (see Fig. 16). In 2010 December, using all ATCA baselines, we successfully demonstrated spectral line observations with 16 × 1 MHz *zoom* channels providing very high velocity resolution, and also pulsar binning mode. High time resolution modes are currently being tested. In Section 6 we present a selection of results obtained during the CABB commissioning week in 2009 April and afterwards.

[4] Previously developed ATNF 8 GS s^{-1} 2-bit sampler chips, as used in the MOPS, were unsuitable for the CABB upgrade. 2-bit sampler systems have significant quantization errors, increasing the noise and causing distortions. While they have adequate RFI rejection at high frequencies, they are unsuitable for the stronger RFI often encountered at lower frequencies. MOPS delivers a maximum bandwidth of 8 GHz, split into four overlapping IFs of 2.2 GHz each. Three modes are provided, giving resolutions of 2.2 MHz, 270 kHz or 34 kHz.

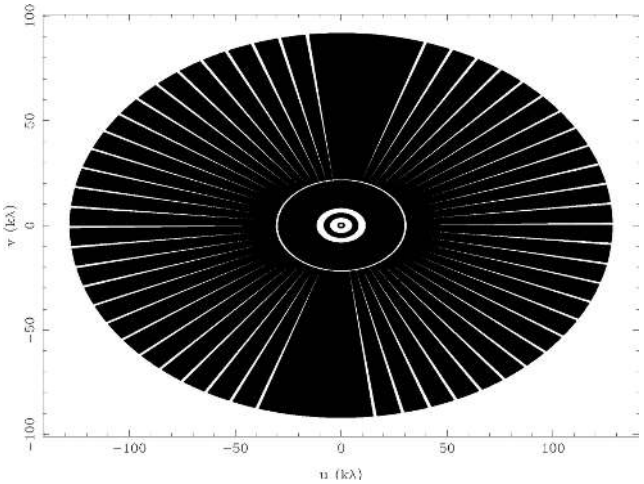

Figure 15. The spectacular *uv*-coverage obtained with CABB 2 GHz bandwidth in a full 12-h synthesis observation. Shown here are projected baseline tracks obtained during an observation of Pictor A (Section 5.3) at 6 cm with the ATCA in the 6A configuration.

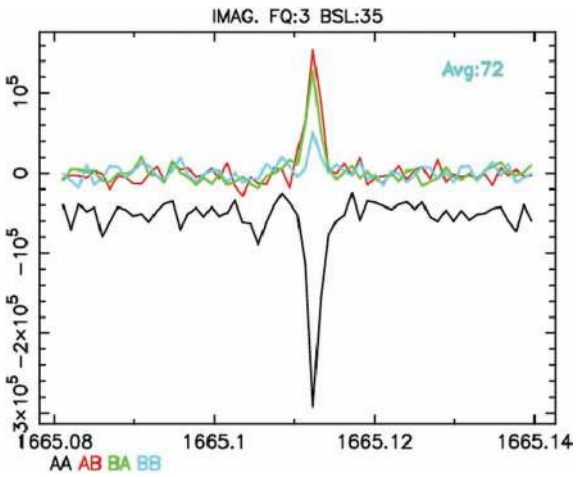

Figure 16. Progress towards *zoom* modes: a single baseline partial *zoom* spectrum of the maser OH 213.705 from ATCA CABB observations on 2010 March 4. Intensity (arbitrary units) is plotted against frequency in MHz. AA, AB, BA and BB are the four polarization products between antennas CA03 and CA05, showing the imaginary part of the cross-correlation so as to highlight the high degree of polarization.

4.2 The primary 2 GHz spectrum

A spectrum over the full bandwidth of 2 GHz is always observed and recorded (strictly 2048 MHz, since all bandwidths and frequency separations are precisely $2n \times 1$ MHz) for both IF bands. All four polarization products are computed, along with the auto-correlations and cross-correlations (interferometer output) for each of the six antennas of the ATCA. The chosen IF bands must be entirely contained within 8 GHz of each other (see Fig. 3 for an overview of the currently available bands). Note that the 2 GHz band edges are defined by an analogue filter (as were the bands of the original ATCA correlator), so that $T_{\rm sys}$ increases gradually (by less than a factor of 2) towards the outermost edges of the band.

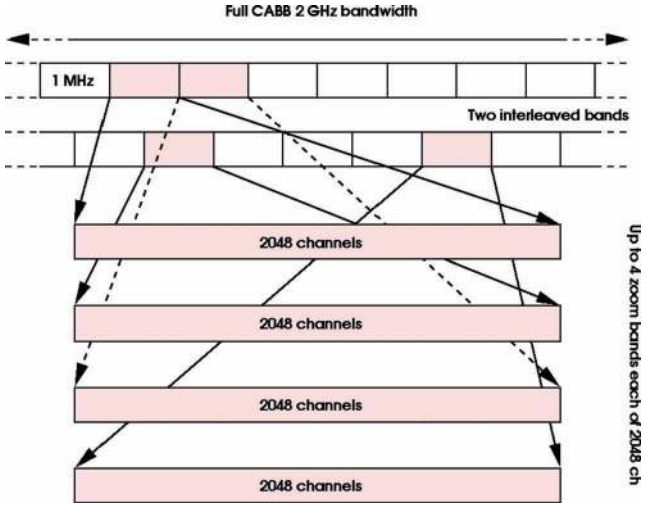

Figure 17. Illustration of a 4 × 1 MHz CABB *zoom* mode setting. CABB internally computes two interleaved bands, each with 2048 channels, and up to 16 *zoom* windows may be selected (in addition to the 2048 channels across the 2 GHz primary band). The interleaved channels, with half-channel offsets, allow flexibility in the positioning of *zoom* bands so that spectral lines do not fall at a channel edge.

For this basic 2 GHz spectrum the maximum resolution is 1 MHz. Each channel has a 'square' response, and thus there are 2048 independent channels across the full spectrum (see Fig. 12). This means that Hann (or 'Hanning') smoothing, which is often used to remove 'ringing', is not required. Internal to the correlator, an output of 4096 channels is routinely computed (i.e. with additional channels interleaved with a half-channel shift) so as to allow flexibility in positioning of *zoom* bands (see Figs 9 and 17). To enable the set-up of *zoom* bands with various widths, the following observing modes are planned for the primary band: 2048 × 1 MHz, 512 × 4 MHz, 128 × 16 MHz and 32 × 64 MHz (see Table 2).

In 2010 December the original 20- and 13-cm band receivers were upgraded to a single 10–30 cm (or nominally 16-cm) band, providing an instantaneous frequency coverage from 1.1 to 3.1 GHz (although the usable bandwidth is reduced by RFI). The new receivers have an improved sensitivity over the original 20- and 13-cm receivers, and include new orthomode transducers, significantly improving the polarization performance towards the top end of the band.

In the 6- and 3-cm bands, which are generally observed simultaneously, the existing front-ends allow a 2 GHz bandwidth to be used for each band (see Fig. 3).

In the 15-mm (previously referred to as 12-mm), 7-mm and 3-mm bands, two IF bands may be selected within an 8 GHz bandwidth. In the 7-mm band, both band centres must be either greater than 41 GHz (the point at which the conversion changes from lower side-band to upper side-band) or less than 41 GHz. For example, methanol lines at 36 and 44 GHz cannot be observed at the same time.

4.3 RFI and bad channels

Single-channel interference spikes are found one-quarter, one-half and three-quarters of the way across the 2 GHz band and are due to the way the interleaved ADC samples are generated (see Section 3.2). When using 2048 channels, these are located in channels 513, 1025 (the centre channel) and 1537. Because they are always contaminated with self-generated interference, the channels are flagged by the correlator before the data are written to disc.

Further interference spikes are commonly observed due to harmonics of the 640 MHz data clock and the 4096 MHz ADC clock. These occur in channels 129, 257, 641, 769, 897, 1153, 1281, 1409, 1793 and 1921 (in 2048 channel mode). The correlator does not by default flag these channels (but can be instructed to) because they are not always correlated.

4.4 CABB cycle time

By default, the correlator writes out one set of spectra every 10 seconds. If required, this interval can be decreased to as little as 1 second. Without *zoom* windows, the correlator will output 3.9 MByte per cycle, which corresponds to a data rate of 1.4 GByte per hour for 10-s cycles. With a full set of zoom windows this rate may increase nearly 20-fold.

4.5 Zoom modes

CABB provides up to 16 *zoom* windows in each of the two selected IF bands; these are in addition to the full 2 GHz primary spectrum. The four basic correlator configurations are listed in Table 2.

In each zoom band, the output will always be 2048 independent non-overlapping channels. Interleaved channels are not computed, but the channels will still be clean 'square' channels, with negligible spillage (i.e. no ringing from narrow lines). The choice of bandwidths for the *zoom* windows is 1, 4, 16 and 64 MHz. Each of the 16 *zoom* windows must be of the same width as the 'continuum channels' selected for the primary 2 GHz spectrum. The channel width of the primary 2 GHz spectrum can be chosen separately for each IF band.

The first full baseline ATCA observations with a CABB *zoom* mode were carried out in 2010 May. Using 8 × 1 MHz *zoom* windows we were able to observe eight methanol maser transitions around 25 GHz (see Section 6.3). This was followed by OH maser observations in 2010 July, with CABB providing full Stokes polarization and high spectral resolution (Caswell & Green 2011). The first observations with 16 × 1 MHz *zoom* windows were obtained on 2010 December 17 (see Section 6.5).

The separation of selected *zoom* windows within the 2 GHz band can be any integral multiple of half the zoom bandwidth. To seamlessly cover a selected band, *zoom* windows need to be interleaved by a half width (see Figs 9 and 17). For example, four interleaved 1 MHz channels cover 2.5 MHz of bandwidth or 16 interleaved 1 MHz channels cover 8.5 MHz of bandwidth (see Section 6.5). Consolidation and normalization of interleaved channels take place in the correlator, before the data are written to disc.

4.6 CABB scheduling

The addition of up to 16 *zoom* windows for each of two IF bands required an upgrade of the ATCA scheduling software. The old scheduler, *atcasched*, a terminal-based schedule creator, could not easily cope with another 32 input parameters. It has been replaced with a web-based scheduler called the *CABBScheduler*. The new scheduler runs as javascript in a browser and was written in java using the *Google Web Toolkit*. It makes use of tabs and stacking to reduce the amount of information presented at once and integrates existing web-based tools like the ATCA calibrator data base and the velocity calculator into the scheduler interface. Behind the scenes it uses server validation of the schedule timing using the same code as the observing program to ensure accurate scheduling. The

scheduler calculates the *zoom* band channels based on the date, source position, velocity and line rest frequency. It also searches for calibrators near the position of interest and displays their characteristics such that an informed selection can be made. While the scheduler is aimed at making it easy to manually create small schedules, there are facilities for bulk import of user-created source catalogues and global search and replace of values. The schedule files are in a simple ASCII format with incremental scan-to-scan changes, making it relatively straightforward to produce large schedules with user-written scripts.

Comprehensive ATCA observing information can be found at www.narrabri.atnf.csiro.au/observing, including a link to the CABB Sensitivity Calculator which is highly recommended to obtain observing characteristics (e.g. rms noise per channel) at specific frequencies and correlator settings.

As the implementation of *zoom* modes proceeds and our experience with CABB observing grows, the *CABBScheduler* is likely to accumulate further options. Most recently, an option to set the channel range for calibration purposes (in particular, delays and $T_{\rm sys}$) was added, with the goal to avoid RFI plagued channels in the respective observing bands.

After a proprietary period of 18 months, ATCA data are publicly available via the Australia Telescope On-line Archive (ATOA) at atoa.atnf.csiro.au.

4.7 CABB observing

The CABB correlator has radically altered the way the telescope operates. Extensive changes have been made to much of the control and monitoring software used by the ATCA, and a summary of these changes is presented here.

The coarse and fine attenuators have been replaced with CABB internal attenuators. The regular mm attenuators remain however, and progress is being made towards having specific attenuators for each cm receiver package as well. These attenuators continue to be controllable through CAOBS. The ATCA monitoring package MONICA has been revised to include all the new CABB monitoring points, and can now also be used to control many of the devices it is attached to. The primary control interface, CAOBS, has remained much the same as for the original correlator, but there are a number of changes. The most important change has been the introduction of separate commands for delay, phase and amplitude calibration at the beginning of an observing run, replacing the automated *cacal* procedure.

A variant of the mosaic observing mode available on the ATCA has been introduced. Observations in the mosaic mode can cover a large contiguous area of sky with numerous pointing centres. The new variant, called OTF mosaicking, reduces the overheads of moving between pointing centres. For OTF mosaicking, the telescope slews continuously, moving the beam by half its width during each correlator cycle. This mode is made attractive with the broad bandwidths provided by CABB, as the integration time can be reduced without incurring the usual slew-settling overheads. In this way the time for each pass of the whole mosaic field is reduced, improving the sampling of the *uv*-plane.

5 CABB DATA REDUCTION

The calibration, imaging and analysis of ATCA data are typically done in MIRIAD. As MIRIAD continues to be actively developed, it is essential that the latest software updates are used to reduce CABB data.

For continuum observations a new calibration strategy has been developed which ensures that amplitude calibration dependence on frequency is accounted for, regardless of the fractional bandwidth covered by the data. All ATCA users are encouraged to consult the MIRIAD Users Guide for the full details of this calibration strategy.

To improve spectral line data calibration, MIRIAD now generates time-variable bandpass solutions that have been found to reduce bandpass calibration errors in the 2 GHz band from 1 per cent to as little as 0.1 per cent. The *zoom* bands themselves have a digitally defined bandpass that is corrected for online, and usually require no further correction during off-line reduction. For gain calibration purposes, MIRIAD treats the zoom bands in the same way as the primary bands.

The greater instantaneous continuum sensitivity of CABB makes it easier to find suitable phase calibrators (close to the target source) and flux calibrators over the full frequency range. For frequencies between 1 and 25 GHz, the preferred ATCA flux calibrator is PKS 1934–638. It has a known, stable flux, no detected linear polarization and only $\sim$0.01 per cent circular polarization (Reynolds 1994; Sault 2003). At high frequencies ($>$50 GHz), the preferred flux calibrator is the planet Uranus. Its flux is known to vary with time, but it does so in a way that is understood and can be modelled (Orton et al. 1986; Kramer, Moreno & Greve 2008). In the 7-mm band (30–50 GHz) either PKS 1934–638 or Uranus may be used, depending on the telescope configuration (in particular baseline length), frequency setup and source elevation. Recent CABB measurements of PKS 1934–638 (and Uranus) in the 7-mm band flux indicate 0.52 (0.70) Jy at 33 GHz and 0.35 (1.17) Jy at 45 GHz.

At frequencies below 10 GHz the increased bandwidth also means a larger number of channels will be affected by RFI, and extensive flagging of the data is required before processing. The flagging capabilities of MIRIAD have been improved in an attempt to deal with this (see Section 5.1). The large fractional bandwidth has to be considered for data reduction below $\sim$10 GHz. One approach is to split the data into several narrow frequency bands, then calibrate and image these separately. Correcting the images for the primary beam response, which varies with frequency (see Fig. 4), is then possible for each sub-band, before combining them to reach the full sensitivity, if required. Alternately, for single-pointing continuum observations at 4–10 GHz, a 2 GHz wide band may be processed in one go as long as the MFS is used for imaging (options *MFS* and *sdb* in the task INVERT) and deconvolution (task MFCLEAN). For observations that require high dynamic range and/or accurate polarization calibration the 'divide and conquer' approach is still expected to yield better results as it can deal with variations in the calibration parameters with frequency.

An ATCA discussion forum (atcaforum.atnf.csiro.au) has been set up for observers to discuss matters relating to CABB observing and data reduction.

Several tasks in the MIRIAD software package (Sault, Teuben & Wright 1995) have been modified and some new tasks have been added. This work will continue over the next few years. It is therefore important to (a) reduce data in the latest version of MIRIAD, (b) read all relevant documentation, (c) check each step, each task and intermediate results carefully and (d) provide feedback to the development team (E-mail: miriad@atnf.csiro.au).

5.1 Modified MIRIAD tasks

Some of the notable changes to MIRIAD tasks are as follows.

(i) The option *rfiflag* in the task ATLOD flags known, persistent RFI, mostly seen in the low-frequency range. The RFI details are

regularly updated and stored in ASCII table which can be downloaded and modified for use in this task. The *birdie* option was updated to flag internal CABB RFI which is fixed in channel number. Both options, *rfiflag* and *birdie*, are recommended when loading CABB data as they eliminate a large fraction of the RFI and facilitate subsequent flagging and data calibration.

(ii) A *maxwidth* parameter was added to the task UVSPLIT to limit the bandwidth of the output files, allowing the data to be processed in smaller frequency chunks.

(iii) The flagging program BLFLAG can now display data from all channels separately using the *nofqav* option.

(iv) Time variability in the bandpass can now be solved for with the task MFCAL. The routines that apply calibration have been updated to interpolate between the bandpass solutions.

(v) The task MFBOOT can now correct the spectral index across the spectrum as well as the flux level when using planets for flux calibration (typically used for mm observations).

(vi) Other tasks, in particular the plotting tasks, received minor updates to cope with larger data volumes, larger numbers of simultaneous frequency bands and much higher frequency resolution compared to that provided by the original ATCA correlator.

5.2 New MIRIAD tasks

Several new tasks have been written by the MIRIAD development team, which include the following.

(i) PGFLAG – a pgplot-based data editing tool (see Fig. 18) replacing the task TVFLAG, an excellent, interactive flagging task which was designed for 8-bit displays.

(ii) MIRFLAG – a task which allows automated flagging of a *uv*-data set (specifically continuum data; see also TVCLIP with options *notv*). It scans the data on a baseline- and channel-dependent basis to find outliers (either in amplitude or based on rms noise) and flags these; it can be instructed to flag small or large clusters of data points. Care should be taken to not accidentally flag astrophysically important spectral lines.

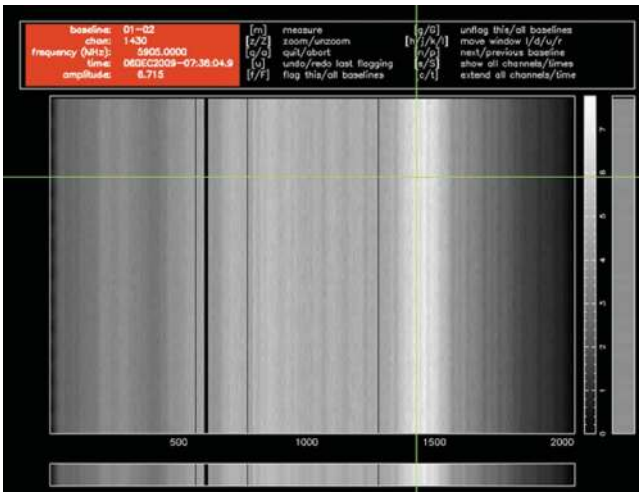

Figure 18. Screen-shot of the new PGFLAG task in the MIRIAD software package (see Section 5.2).

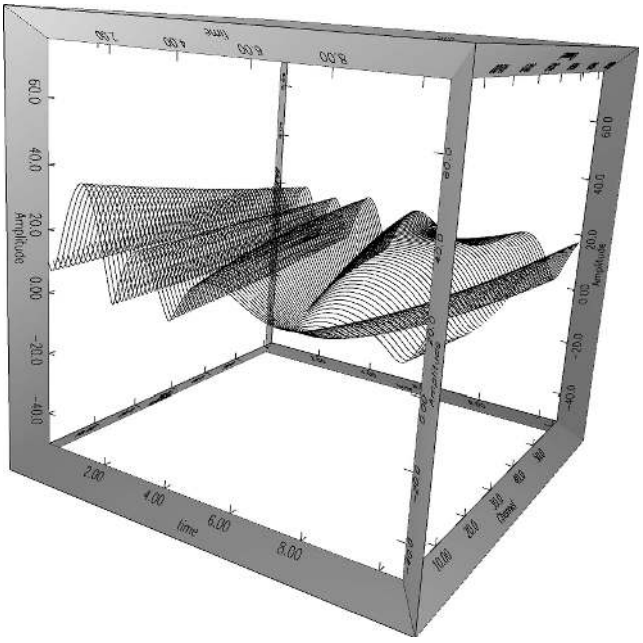

Figure 19. Visibility amplitudes varying over time and frequency for CABB observations of the nearby FR-II radio galaxy Pictor A (Section 5.3). The plot is generated using the interactive tool PLOTVIS and shows visibility amplitudes for a single baseline (CA02–CA03) of a 10-h observation with a single 2 GHz bandwidth between 4.5 and 6.5 GHz, averaged into 64 × 32 MHz channels.

(iii) PLOTVIS – provides an interactive, three-dimensional view of the visibilities (see Fig. 19).

5.3 Example: the radio galaxy Pictor A

The large bandwidth (divided into a large number of channels) now available with CABB provides a hugely improved *uv*-coverage for any single observation when MFS is utilized (see Fig. 15). The almost-complete coverage reduces the need, in many instances, to observe the target with multiple ATCA configurations and thus alleviates issues associated with source variability and calibration differences between observations. However, care must be taken when imaging large or complex sources and sources with significant spectral variation. Large and complex sources, such as the nearby Fanaroff & Riley type-II (FR-II) galaxy Pictor A (Fig. 20), introduce large variations in complex visibilities not only in time but also in frequency. Figs 21(a) and (b) show the spectral plot at a given time and the amplitude visibility plot versus time. The time–frequency variability of the visibility amplitudes can more easily be seen using the new PLOTVIS tool (see Fig. 19) which provides an interactive, three-dimensional view of the visibilities. Spectral differences between the various components of the source, i.e. the lobes, hot-spots, jet and the core, further complicate imaging and necessitate the use of multi-frequency deconvolution algorithms such as MFCLEAN.

6 CABB RESULTS

CABB operations and scientific commissioning interleaved with engineering and maintenance blocks were carried out between 2009 April 10 and 21. Here, we report on some of the results obtained during this period as well as more recent observations.

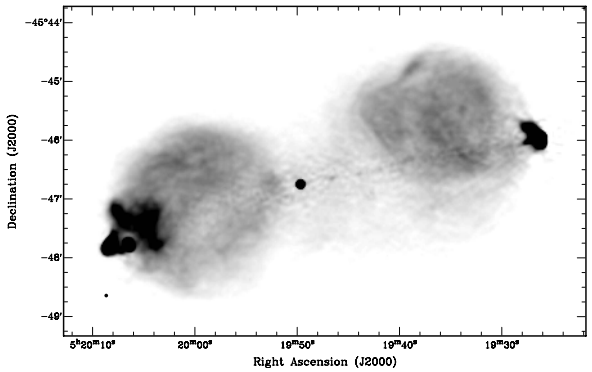

Figure 20. ATCA 6-cm radio continuum image of the double-lobe radio galaxy Pictor A made with CABB using 2 GHz of bandwidth. In this image, made using observations in the 6A array (2009 June 17), 6D array (2009 August 30) and EW352 array (2009 December 06) Lenc et al. achieved a dynamic range of 38 000:1 and an angular resolution of 2.2 arcsec. Pictor A's complex structure, i.e. its extended lobes, multiple hot-spots, narrow jet and bright core present many imaging challenges (for more details see Section 5.3).

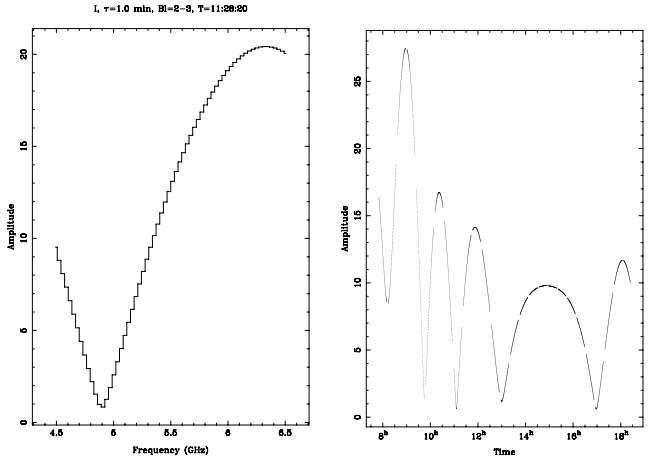

Figure 21. Left: spectral plot of Pictor A amplitude visibilities at a given time for a single ATCA baseline (CA02–CA03) of a 10-h observation using CABB with a single 2 GHz band between 4.5 and 6.5 GHz, averaged into 64 × 32 MHz channels. Right: plot of amplitude versus time for the same observation.

6.1 Star formation in the G305 H II region

The G305 star-forming region is one of the most luminous H II regions in the Galaxy, centred on the open clusters Danks 1 and 2 and the Wolf–Rayet star WR 48a (Clark & Porter 2004). This complex, which extends over roughly 1 deg^2, is located at l, b = 305°, 0° and a heliocentric distance of ∼4 kpc, which places it in the Scutum Crux arm. The central clusters have ages of about 3–5 Myr and are located in the centre of a large H II region, surrounded by molecular gas and dust. There are numerous infrared hot-spots and massive young stellar objects (Urquhart et al. 2008), ultra-compact (UC) H II regions and molecular masers located on the periphery of the H II region. The integrated radio flux is indicative of >30 deeply embedded 07V stars (Clark & Porter 2004). The detection of these high-mass star formation tracers, within the boundary layer between the ionized and molecular gas, would suggest that, not only are high-mass stars currently forming, but their formation may have been triggered through the interaction of the ionization front and surrounding molecular material.

A multi-wavelength observing program was designed to study the star formation across the G305 complex. High-frequency radio continuum observations are a key ingredient of this program as they allow the large-scale structure of the ionized gas to be traced, and the emission from very young high-mass stars to be identified via their compact and ultra-compact H II regions. Previous cm continuum observations either have covered small areas at high resolution, e.g. around the methanol masers listed in Walsh et al. (1998), or have been of low angular resolution and sensitivity (Danks et al. 1984, Caswell & Haynes 1987, Haverkorn et al. 2006). Mapping large Galactic star-forming regions on the scale of G305 at high-frequency and sub-arcminute resolution has only recently been made possible with the commissioning of CABB on the ATCA. This is primarily due to the factor of at least 16 increase in frequency bandwidth, which effectively increases mapping speeds by the same factor over the previous system to reach the same sensitivity. A further speed increase is gained by the potential to map two frequencies simultaneously using the two IFs.

G305 was mapped using ATCA with CABB at two frequencies (centred around 5 and 9 GHz), requiring 357 separate mosaic points to cover the whole region. Multiple array configurations were required to obtain sufficient *uv*-coverage to recover both extended and compact structures. In total, six different configurations were used to obtain fairly uniform baseline coverage between 30 m and 6 km, which provides sensitivity to angular scales of a few arcsec to a few tens of arcmin. The observations were made in snapshot mode, i.e. 6–8 × 10 s integrations were spent on each of the 357 pointings. This was repeated for each configuration; the total integration time for the project was 75 h.

In Fig. 22 we present a three-colour mid-infrared image of G305 overlaid with contours of the integrated 6-cm emission obtained from the three ATCA hybrid arrays (H75, H168 and H214); these configurations primarily consist of short baselines and so are very sensitive to the large-scale structure of the ionized gas. The ionized

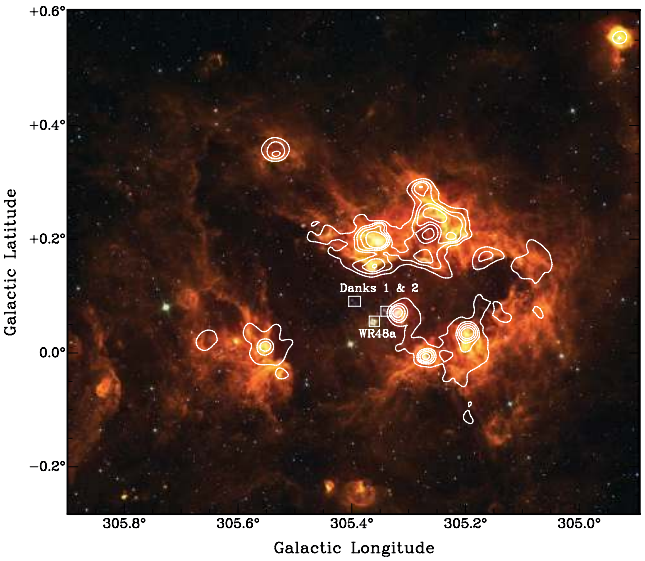

Figure 22. ATCA 6-cm radio continuum emission (contours) of the giant H II region complex G305 overlaid on to a three-colour *Spitzer* Galactic Legacy Infrared Mid-Plane Survey Extraordinaire (GLIMPSE) image (using the IRAC 4.5, 5.8 and 8.0 μm bands coloured blue, green and red, respectively, obtained from the Galactic plane survey by Benjamin et al. 2003). The continuum emission traces the distribution of ionized gas associated with the H II region complex.

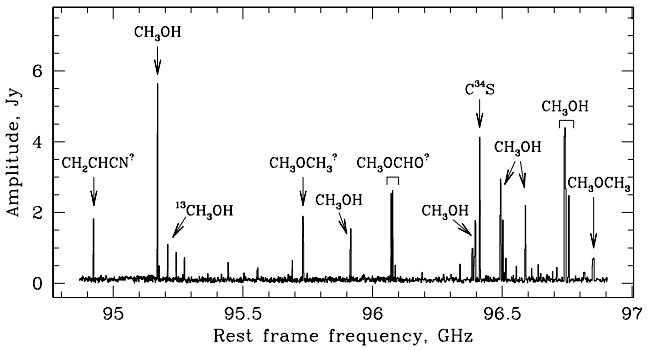

Figure 23. CABB 3-mm broad-band molecular line spectrum of the hot-core chemistry forest associated with NGC 6334 I (see Section 6.2). The spectrum extends from about 95 to 97 GHz; more than 30 molecular lines are easily detected.

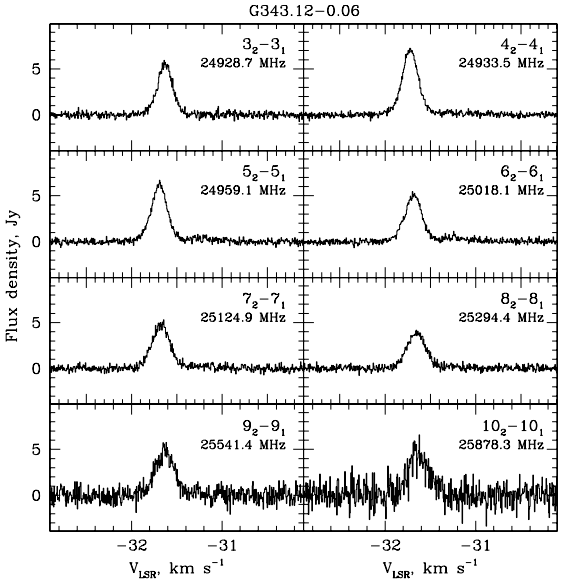

Figure 24. Methanol maser lines in the high-mass star-forming region G343.12–0.06 around 25 GHz, as observed with eight CABB 1 MHz *zoom* windows. The full width of each *zoom* window is 12 km s^{-1} and the velocity resolution is 6 m s^{-1}.

gas is correlated with prominent emission structures seen in the mid-infrared, tracing the interface between the H II region and surrounding molecular gas. Combining the radio emission with tracers of molecular gas (e.g. Hindson et al. 2010) and dust will allow investigating the impact of massive stars associated with Danks 1 and 2 on the structure of G305's molecular gas as well as its influence on current and future star formation in the region.

6.2 A forest of molecular lines from NGC 6334 I

NGC 6334, also known as the 'Cats Paw Nebula', is a giant molecular cloud/H II region located at a distance of ∼1.7 kpc in the southern Galactic plane. Situated in its northern part is the high-mass star-forming site known as NGC 6334 I. This site contains a hot molecular dust core at the head of a bright cometary UC H II region and is associated with a wealth of young high-mass star-forming phenomena such as masers, molecular outflows, a forest of molecular line hot-core chemistry as well as several compact millimetre continuum sources (e.g. Hunter et al. 2006; Beuther et al. 2007). Walsh et al. (2010) studied a 5 × 5 arcmin^2 region encompassing NGC 6334 I and another bright (sub)millimetre continuum source further north [NGC 6334 I(N)] at λ 3 mm (from 83.5 to 115.5 GHz) using the 22-m Mopra telescope (angular resolution ∼36 arcsec). They detect a total of 52 transitions from 19 species (molecules, ions and radicals). Beuther et al. (2008) studied NGC 6334 I with the ATCA in 2006 (pre-CABB) at around 88.4 GHz, achieving an rms of 23 mJy beam^{-1}. While the angular resolution was high (2.3 × 1.6 arcsec^2), the modest observing bandwidth of 128 MHz only permitted two molecular emission lines to be detected simultaneously.

NCG 6334 I was again observed on 2009 April 16, as part of the CABB science commissioning program. Antenna array configuration H168 was used with an on-source observing time of 1.6-h. Fig. 23 shows the 2 GHz wide-band CABB spectrum (95–97 GHz) towards the central position of NGC 6334 I at α, δ(J2000) = $17^h\,20^m\,53\overset{s}{.}35, -35^\circ\,47'\,1\overset{''}{.}6$. More than 30 molecular lines are easily detected simultaneously, demonstrating the power of the CABB for multi-transition chemical line studies.

6.3 Galactic methanol maser observations

Fig. 24 demonstrates the power of CABB with its first zoom modes (obtained on 2010 Jun 3 by Maxim Voronkov). Eight zoom windows were chosen to cover bright methanol maser transitions near 25 GHz ($J_2 - J_1$ E methanol series) in the high-mass star-forming region G343.12–0.06 (IRAS 16547−4247). This source has a jet-driven molecular outflow embedded in a molecular cloud (Brooks et al. 2003). The interaction between the outflow and the cloud produced a number of masers across the region (Voronkov et al. 2006). The CABB observations shown here replicate in a more efficient way most of the 25 GHz observations from Voronkov et al. (2006) which were obtained with the original ATCA correlator by cycling through all the transitions sequentially (a stronger $J = 10$ transition was observed instead of a weak $J = 2$ maser reported in the original study). Each zoom window was 1 MHz wide (about 12 km s^{-1} of velocity coverage) and had 2048 spectral channels, providing a spectral resolution of about 6 m s^{-1}. Even the narrow maser lines were notably oversampled, as the spectral resolution provided by this CABB configuration was a factor of 4 to 8 times better than that of Voronkov et al. (2006).

6.4 The β Pictoris debris disc

Debris discs represent the final evolutionary phase of protoplanetary discs around young stars. They are optically thin, contain little or no gas and are generally thought to be in the final planet forming stage (Wyatt 2008). At a distance of just 19.3 pc (Crifo et al. 1997), the β Pictoris debris disc is an excellent target for high-resolution imaging.

β Pictoris has been extensively studied since its discovery as an infrared excess star by *IRAS* (Aumann 1984) and subsequent imaging of its dusty disc by Smith & Terrile (1984). The latter revealed a nearly edge-on disc ∼400 au (20 arcsec) in extent. At an age of 10–20 Myr (Zuckerman et al. 2001), β Pic is mature enough to host planets and, indeed, the direct detection of an ∼8 Jupiter mass planet was recently reported (e.g. Lagrange et al. 2010).

Modelling of the thermal and scattered light by Artymowicz (1997) indicates that the β Pic disc contains a wide range of grain sizes from sub-micron through to at least millimetre dimensions. Simple order of magnitude estimates show that even the smaller dust grains cannot be primordial because they would be blown away

radiatively on time-scales of tens of orbits. Collisions between larger bodies will lead to fragmentation, since there is very little gas to dampen the relative grain velocities (Lecavelier des Etangs et al. 2001), and thus these collisions act to replenish the dust. Debris discs can have a very different appearance at different wavelengths. Sub-mm and mm observations trace the largest grains, which are least affected by stellar radiation, suggesting that these grains are the best probe for the larger parent bodies responsible for the dust production.

Millimetre interferometry provides high angular resolution and much needed information on the largest grain populations in debris discs. The close proximity of β Pic and its southern declination make it an ideal target for mm-imaging with the ATCA.

Using CABB 3-mm (92–96 GHz) and 7-mm (42–46 GHz) observations with the ATCA in the H214 configuration, Maddison & Wright (in preparation) were able to clearly resolve the debris disc of β Pic (see Fig. 25). These are the longest wavelength detections of any debris disc obtained to date. To achieve the 4 GHz wide bandwidth, they placed the two 2 GHz IF bands adjacent to each other; integration times were 8 h at 3 mm (2009 September 12/13) and 6.5 h at 7 mm (2009 September 13/14). Maddison & Wright (in preparation) found clear evidence of structure within the dust and a direct detection of inner disc clearing, in agreement with recent Sub-Millimetre Array (SMA) 1.3-mm observations by Wilner, Andrews & Hughes (2011).

6.5 Water masers in the Sgr B2

In 2010 December, the first CABB observations with 16 × 1 MHz *zoom* channels were successfully demonstrated. Fig. 26 shows the high-velocity resolution line data of water masers in Sgr B2. Here the *zoom* channels are overlapped in 0.5 MHz steps to obtain a uniform spectrum over 8.5 MHz of bandwidth with a velocity resolution of 7 m s^{-1}. McGrath, Goss & De Pre (2004) show a similar spectrum at 0.66 km s^{-1} velocity resolution, while Reid et al. (2009) determined the trigonometric parallax of Sgr B2 by measuring the H_2O maser positions with the Very Large Baseline Array (VLBA) over 1 year.

6.6 The Circinus Galaxy

The Circinus Galaxy is, at a distance of 4 Mpc, one of the closest active galaxies. Discovered relatively recently (Freeman et al. 1977) and obscured by Galactic foreground stars and dust, it nevertheless remains a prominent observing target at a large range of frequencies. It harbours an active galactic nucleus (AGN) surrounded by a star-forming ring, an extended stellar disc, double radio lobes (orthogonal to the disc) and an enormous H I gas envelope (Jones et al. 1999; Curran, Koribalski & Bains 2008). Bauer et al. (2008) discovered a supernova, named SN1996cr, located just 25 arcsec south of the AGN, adding to the continuing interest in this spectacular galaxy (see Fig. 27).

CABB 6-cm observations were carried out in 2009 April using the EW352 array. The 2 GHz band, centred at 5500 MHz, was divided into 2048 channels. During the 9-h synthesis we regularly observed the nearby calibrator PKS 1352−63. The bandpass and amplitude calibrator PKS 1934−638 were observed at the start of the session. Radio interference was detected in numerous channels, particularly around 5600 MHz (bandwidth 6 MHz) probably related to the 5625 MHz weather radar near the town of Moree. Our goal was to reproduce (or enhance) the 6-cm radio continuum map of the Circinus galaxy obtained by Elmouttie et al. (1998), to study

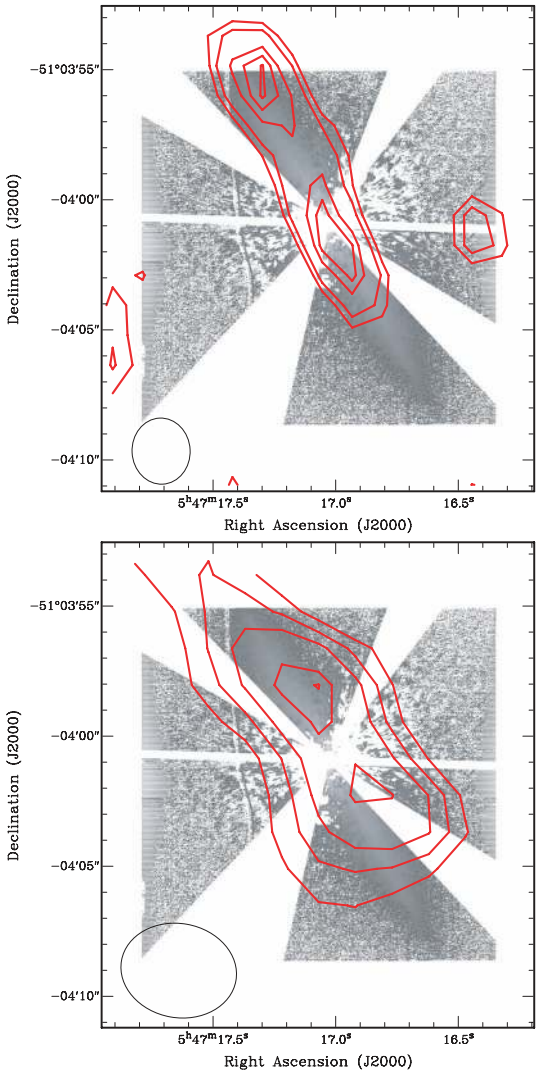

Figure 25. The β Pictoris debris disc (at a distance of 19.5 pc 1 arcsec corresponds to 20 au). Contours show the extended radio continuum emission from the dust grains in the disc at 3 mm (top) and 7 mm (bottom) overlaid on to an ESO/NACO *H*-band (1.65 μm) image in grey-scale (Boccaletti et al. 2009). The radio data were taken with the ATCA in the H214 configuration, using CABB with 4 GHz of bandwidth. The contour levels are 1.5, 2, 3, 3.5 and 4σ (where σ = 95 μJy is the rms noise) at 3 mm (beam ≈2.5 arcsec) and 2, 3, 4, 5 and 6σ (where σ = 21.8 μJy) at 7-mm (beam ≈4.5 arcsec). The NE peak appears brighter than the SW peak in both images (see Section 6.4).

the emission from the nuclear region, the disc and the radio lobes. Their published ATCA data consisted of 5 × 12 h with a bandwidth of 128 MHz, reaching an rms of 120 μJy beam^{-1}. With an effective increase of a factor of 20 in the useable bandwidth (20 × 100 MHz), a factor of ∼2 in T_{sys}, highly improved uv-coverage and dynamic range, we estimate a theoretical noise of ∼13 μJy beam^{-1} for the CABB 6-cm imaging of the Circinus galaxy ('uniform' weighting). The data were calibrated in MIRIAD by splitting the 2 GHz band into 64 × 32 MHz channels, then imaged and further calibrated in DIFMAP (Shepherd 1997) using a combination of model-fitting and self-calibration. The resulting image (uniformly weighted; no self-calibration) is shown in Fig. 27. In the nuclear region the AGN and the supernova SN1996cr are clearly detected (and well-resolved in the high-resolution image, not displayed here). Thanks to CABB,

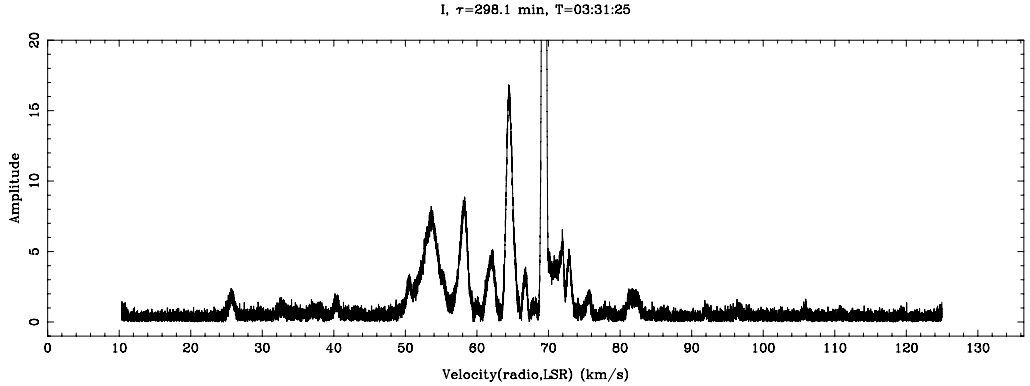

Figure 26. High-velocity resolution CABB spectrum of water masers in Sgr B2, taken on 2010 December 17 (uncalibrated). Here 16 × 1 MHz *zoom* channels were concatenated, i.e. overlapped in 0.5 MHz steps, to give 17 408 channels over 8.5 MHz bandwidth; the velocity resolution is 7 m s^{-1}. Note that at the outermost edges of the concatenated band T_{sys} gradually rises by less than a factor of 2.

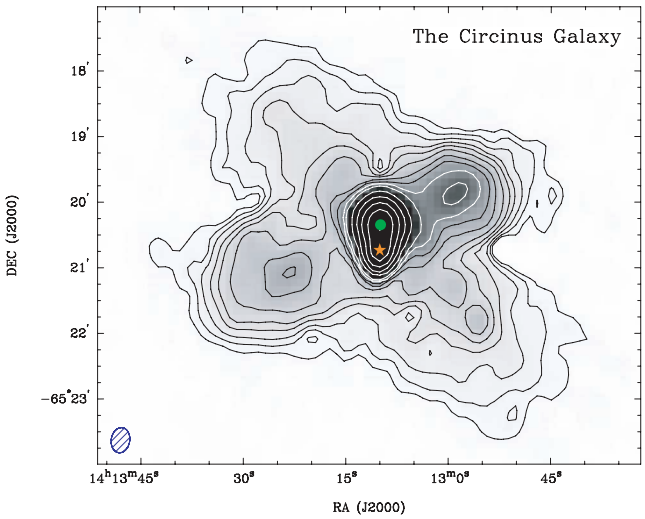

Figure 27. ATCA 6-cm radio continuum emission of the nearby Circinus Galaxy (observed on 2009 April 2, EW352 array, CABB 2 GHz bandwidth). We detect the AGN (marked with a green dot), the recent supernova (SN1996cr; marked with an orange star), the inner galaxy disc ($PA = 223°$) and the orthogonal radio lobes ($PA = 115°$). Contour levels are 0.3, 0.5, 0.8, 1.3, 1.8, 2.6, 3.8, 5, 7, 10, 20, 40, 80, 160 and 320 mJy beam^{-1} (white contours start at 7 mJy beam^{-1}). The synthesized beam (23 × 17 arcsec^2) is displayed in the bottom-left corner. For more information see Section 6.6.

the extended, star-forming disc of the Circinus galaxy and its spectacular radio lobes are revealed in detail (the image dynamic range is ∼1000:1). Our CABB 6-cm image closely resembles the pre-CABB 20-cm image by Elmouttie et al. (1998). An in-depth analysis of the gas distribution and star formation in Circinus is under way (For, Koribalski & Jarrett, in preparation).

6.7 The Radio Galaxy NGC 612

NGC 612 (PKS 0131−36) is one of the nearest powerful radio galaxies ($z = 0.0297$; e.g. Ekers et al. 1978). Its eastern radio jet shows a hot-spot, typical for Fanaroff & Riley type-II radio sources. The host galaxy is a dust-lane S0 with a young stellar population detected along its disc (Goss et al. 1980; Véron-Cetty & Véron 2001; Holt et al. 2007). NGC 612 also contains a large-scale disc of H I gas (140 kpc in diameter) as well as a faint bridge-like H I structure (∼400 kpc in size) that stretches towards a gas-rich companion (Emonts et al. 2008). The proximity of NGC 612 allows us to have a close look into the physical processes associated with powerful radio galaxies.

The complex and bright structure of the radio continuum source (roughly the size of the primary beam at 6 cm) made NGC 612 an excellent target to image during CABB commissioning. On 2009 April 9 and 10, NGC 612 was the first science target observed simultaneously in the 3- and 6-cm bands, using the H168 hybrid configuration. Over the following months, these observations were repeated in H75 and H168 at three additional epochs. The main aims were to perform wide-band imaging across the primary beam, derive instantaneous spectral index information of both the nucleus and hot-spot across a large frequency range and investigate CABB's performance for deriving polarization properties of this source.

Fig. 28 shows preliminary results obtained from the CABB observations of NGC 612. It includes total intensity images of its radio continuum emission at 3 and 6 cm and a spectral index diagram (over 4 GHz) of both its nucleus and eastern hot-spot. For the latter, each individual data point was obtained by extracting 128 MHz sub-bands from the full CABB 2 GHz band. Standard reduction was performed on each 128 MHz sub-band (i.e. bandpass/phase/flux calibration, imaging, cleaning and primary beam correction; see Section 5 for details). We then measured the integrated flux densities of the nucleus and the eastern hot-spot by fitting Gaussian functions in each '128 MHz' sub-image. The steep spectral index of the eastern radio hot-spot[5] is in stark contrast to the rather flat spectrum of the nucleus (at 6-cm the continuum of the inner radio lobes becomes too bright to clearly distinguish the resolved nucleus). These results are in agreement with continuum observations at 20 GHz by Burke-Spolaor et al. (2009). The wealth of spectral index information that can be obtained with a single CABB observation, once the calibration is finalized, is striking. The preliminary analysis also indicates that the eastern hot-spot is highly polarized (∼25 per cent) at 6 cm.

6.8 Deep continuum observations of the ECDFS

The Extended Chandra Deep Field South (ECDFS) is part of the Australia Telescope Large Area Survey (ATLAS; Norris et al. 2006).

[5] In Fig. 28 the spectral index of NGC 612's eastern hot-spot is plotted using linear rather than logarithmic axes in order to better visualize the instantaneous frequency coverage of CABB.

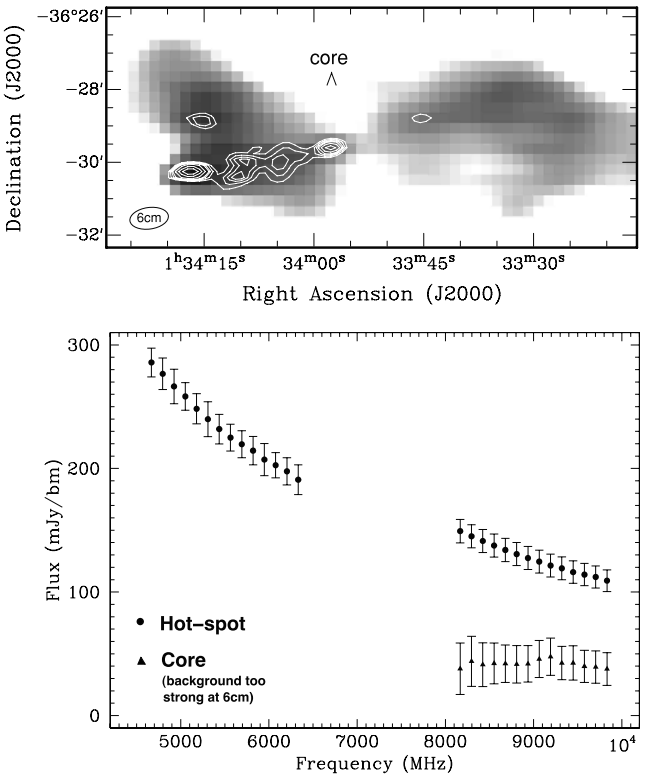

Figure 28. The radio galaxy NGC 612 (PKS 0131−36) as observed at 3 and 6 cm during CABB commissioning in 2009 April with the ATCA in the compact H168 antenna configuration. Top: preliminary radio continuum image at 6 cm (grey-scale) and 3 cm (contours). The contour levels are 4, 7, 10, 13, 20, 30 and 40 mJy beam^{-1}. Bottom: spectral index of the eastern hot-spot (dots) as well as the nucleus (triangles) across the full 2 × 2 GHz range of the two bands. The frequency separation between consecutive data points reflects the 128 MHz bandwidth of the original ATCA correlator. The spectral index properties are visualized using linear rather than the commonly used logarithmic axes (see Section 6.7 for details).

The goal of ATLAS is to study the origin and evolution of both star-forming and AGN-dominated galaxies by making deep multi-wavelength radio observations complemented by deep infrared and optical imaging as well as spectroscopy.

The ECDFS was observed for about 4 hours in the ATCA H168 configuration on 2009 April 19. The 2 GHz CABB band was centred at 5500 MHz and divided into 2048 channels. The data were processed in MIRIAD, initially using the full 2 GHz spectrum. Without self-calibration, an rms noise of 23 μJy was obtained (see Fig. 29); this was improved to 16 μJy (close to the theoretical rms) after one iteration of phase self-calibration. Re-processing and primary beam correction in smaller sub-bands (e.g. 128 MHz) will be required to obtain correct flux densities and spectral indices for all sources in the field.

Source S415, located several arcmin from the pointing centre, is an example of the rare 'Infrared-faint Radio Sources' published by Norris et al. (2006) (see also Beswick et al. 2008). Using ATLAS data, Middelberg et al. (2011) give its 20-, 13- and 6-cm flux densities as 2.64 ± 0.54 mJy, 0.70 ± 0.08 mJy and <0.33 mJy, respectively, resulting in a spectral index of $\alpha_{20,13} = -2.38 \pm 0.43$. The CABB 6-cm data reveal a ≈80 μJy radio source at the position of S415, confirming the steep spectral index. This is important since such sources are often associated with high-redshift radio galaxies (Krolik & Chen 1991; de Zotti et al. 2010). S415 has no detected

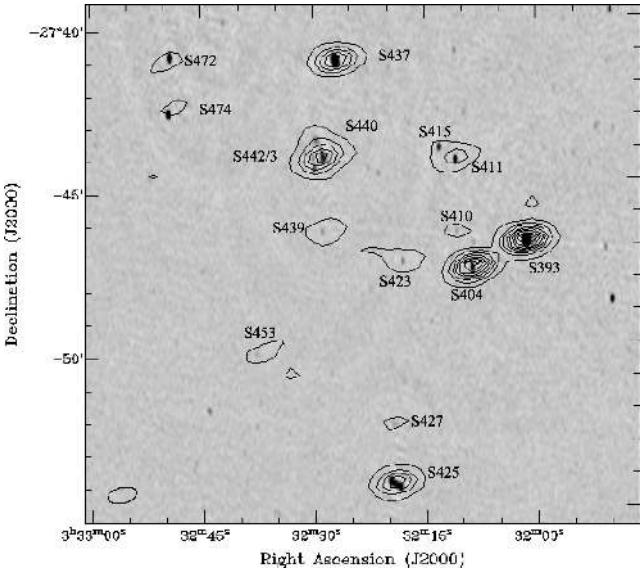

Figure 29. Preliminary CABB radio continuum image of the ECDFS at 6-cm (contours) overlaid on to a pre-CABB 20-cm image (grey-scale) from Hales et al. (2011). Contours are at intervals of ≈100 μJy. The 20-cm data were taken with the ATCA in a 6-km configuration, while the 6-cm data were observed in the compact H168 array.

3.6 μm counterpart to a limit of ∼1 μJy, giving it a $S_{20\mathrm{cm}}/S_{\mathrm{FIR}}$ ratio of ∼2000, compared to ∼200 typical for radio-loud quasars and ∼10 for star-forming galaxies.

6.9 High-redshift CO

A crucial component in the study of star formation throughout the Universe is a detailed knowledge of the content and properties of the molecular gas. An excellent tracer for molecular gas is the emission-line of carbon monoxide (CO), which is strong enough to be observed out to high redshifts. However, since the first detection of CO at $z > 2$ by Brown & Vanden Bout (1991), observations of molecular gas at high redshifts have been limited by the fact that, at the high observing frequency of CO ($\nu_{\mathrm{rest}} = 115$ GHz for the lowest rotational transition), existing narrow-band receivers covered a velocity range that was generally not much larger than the CO linewidth or the accuracy of the redshift. Moreover, the lack of millimetre receivers in the 20–50 GHz regime resulted in a focus on observations of the higher order rotational transitions. While the higher order transitions are good tracers for the molecular gas that is dense and thermally excited, large reservoirs of low-density and widely distributed gas could be hiding in the lower rotational CO transitions (e.g. Papadopoulos et al. 2000, 2001).

In its coarsest spectral line mode, the 2 × 2 GHz CABB bands with 1 MHz spectral resolution are ideal for targeting high-z CO lines, in particular regarding the lower order transitions that are shifted into the ATCA 7- and 15-mm bands. For example, a source at $z = 3.8$ can be observed in CO(1–0) at 24 GHz (15-mm band) as well as CO(2–1) at 48 GHz (7-mm band), with observations of the latter covering a velocity range of more than 12 000 km s^{-1} per 2 GHz band at a resolution of ∼6 km s^{-1}.

The first detection of high-z CO with CABB was made by Coppin et al. (2010), who detected the CO(2–1) transition in a distant sub-millimetre galaxy at $z = 4.76$, indicating the presence of ∼1.6 × 10^{10} $M_\odot$ of molecular gas. Recently, Emonts et al. (2011a) detected the CO(1–0) transition in a powerful radio galaxy at $z \sim 2$,

representing $\sim 5 \times 10^{10}$ $M_{\odot}$ of molecular gas. This is only the third known high-z radio galaxy detected in CO(1–0), after detections in two others at a significantly lower signal-to-noise ratio levels (Greve, Ivison & Papadopoulos 2004; Klamer et al. 2005). These initial results show the enormous advantage CABB delivers for ATCA studies of molecular gas and star formation in the Early Universe. The excellent performance of CABB for high-z CO observations is demonstrated by Emonts et al. (2011b), including a detailed description of their observing strategy for millimetre spectral line work with CABB.

6.10 Polarization synthesis

The large frequency bandwidths that have become available with CABB are also useful for radio polarization observations, which can tell us about the properties of magnetic fields in the Milky Way and beyond. In particular, the Faraday rotation, an effect where the plane of polarization of a radio wave is rotated when the wave passes through an ionized region with an embedded magnetic field, has been a very popular method over many years (Gaensler et al. 2005; Brown et al. 2007). The Faraday rotation strongly varies with the observing wavelength ($\propto \lambda^2$), which means that the polarization vectors at different frequencies will have different orientations. The magnitude of this variation with frequency (known as the 'rotation measure' or RM) depends on the magnetic field strength and the free electron density in the column that the radio wave passes through. From the measured RM we can estimate the magnetic field strength, if we can correct for the electron density contribution to RM.

A large observing bandwidth gives a great improvement in sensitivity, also in polarization, but only if we can correct for the change in orientation of the polarization vectors with frequency, which is the result of the Faraday effect. By simply summing the different frequency channels some of the polarized signal will be lost if the polarization vectors have different orientations. The novel technique of rotation measure synthesis (or 'RM synthesis'; Brentjens & De Bruyn 2005[6]) helps us out: if the Faraday effect rotates the polarization vectors as a function of frequency, then by choosing the correct RM for that line of sight the polarization vectors can be derotated (in RM synthesis-speak the RMs are referred to as 'Faraday depths'). This way the polarization vectors from all the frequency channels in the observing band can be combined, and the noise level is thus greatly reduced. Typically, one would use many trial Faraday depths and calculate how much polarized flux is recovered at each Faraday depth, to find the Faraday depth of the polarized emission for a particular line of sight. Furthermore, when there are regions along the line of sight that emit polarized radiation with different Faraday depths (e.g. when there is additional Faraday rotation between the emission regions), then each Faraday depth will produce a polarization vector that rotates at a specific rate as a function of observing frequency. The RM synthesis can separate such regions, since it is essentially a Fourier transform. This way RM synthesis adds a depth dimension to measurements of the Faraday effect.

To study whether magnetic fields are important for the evolution of the Galactic supershell GSH287+04–17 we used CABB 20-cm data in combination with RM synthesis. For this purpose we determined Faraday depths of extragalactic sources that are seen through the wall of the supershell, and we compared these to the Faraday depths of extragalactic sources that lie just outside the shell wall. Fig. 30 shows the polarized intensities and polarization angles that were derived for one such source and the polarized intensity that is recovered for different trial Faraday depths. In this example, the extragalactic source is the only source of polarized emission along the line of sight, and the expected response from RM synthesis (similar to the dirty beam in synthesis imaging), which is indicated with a thick red line, closely matches the measured response. We determined the Faraday depths of $\sim$100 extragalactic sources that are seen through or close to the ionized inner part of the supershell wall. The enhanced free electron density will naturally lead to an increase in RM if the magnetic field remains the same. However, we did not find such an enhancement of the RMs of the extragalactic sources here, but we did find a narrow filament that runs nearly parallel to the Galactic plane, where the RM varies by $\gtrsim$250 rad m^{-2}. This filament spans the entire width of the area we surveyed (and is therefore $\gtrsim 5^{\circ}$ wide) but it is only 1° high. Since there appears to be no enhancement in the Hα intensity that is associated with this ribbon it must be magnetic in origin, and it will be very interesting to investigate how such a magnetized structure can have survived in the Galactic interstellar medium.

6.11 AT20G quasar study

Mahony et al. (in preparation) observed a sample of over 1100 quasi-stellar object (QSOs) to study their radio luminosity distribution, a subject that has long been debated in the literature (e.g. Kellermann et al. 1989; Cirasuolo et al. 2003). QSOs are often separated into two categories; 'radio-loud' and 'radio-quiet', but the dividing line between these two classes remains unclear. The increased bandwidth of CABB, and hence increased sensitivity compared to the original ATCA correlator, allows a large sample of objects to be observed in a smaller amount of time, whilst also probing further into the 'radio-quiet' regime. A more detailed description of the observing program is given in Mahony et al. (2010b). Targets were selected from the RASS–6dFGS catalogue (Mahony et al. 2010a); a catalogue of 3405 AGN selected from the *ROSAT* All Sky Survey (RASS) Bright Source Catalogue (Voges et al. 1999) that were observed as part of the 6dF Galaxy Survey (6dFGS; Jones et al. 2009). The observations were carried out in snapshot mode using a hybrid array (H168) on the ATCA from 2008 to 2010, using a two-step process. First, all sources were observed for 2×40 seconds reaching an rms noise of $\sim$0.2 mJy. Secondly, non-detections were re-observed for 2×5 min, reaching an rms noise of $\sim$0.1 mJy.

Preliminary results are shown in Fig. 31 which compares the 20 GHz flux densities (versus redshift) of the X-ray selected sample achieved pre-CABB and with CABB (since 2009 March). It highlights the significant increase in sensitivity that CABB has achieved in comparison to the original correlator.

6.12 Surprising SZ results for two clusters

Pre-CABB, no Sunyaev–Zeldovich (SZ) observations with resolution better than a few arcmin were possible. Even for rich clusters of galaxies many days of integration were required to marginally detect the low brightness SZ dip.

This all changed with the increased sensitivity provided by the CABB system. Two independent observations of different galaxy clusters made with CABB at 18 GHz detected the SZ dip with sub-arcmin resolution and in both observations the SZ was displaced from the peak of the X-ray emission from the cluster gas.

Massardi et al. (2010) observed CL J0152−1357, a massive cluster at $z = 0.83$, and concluded that the cluster was still recovering

[6] RM synthesis was developed independently in 1996 by De Bruyn (NFRA note 655) and by Killeen et al. (1999).

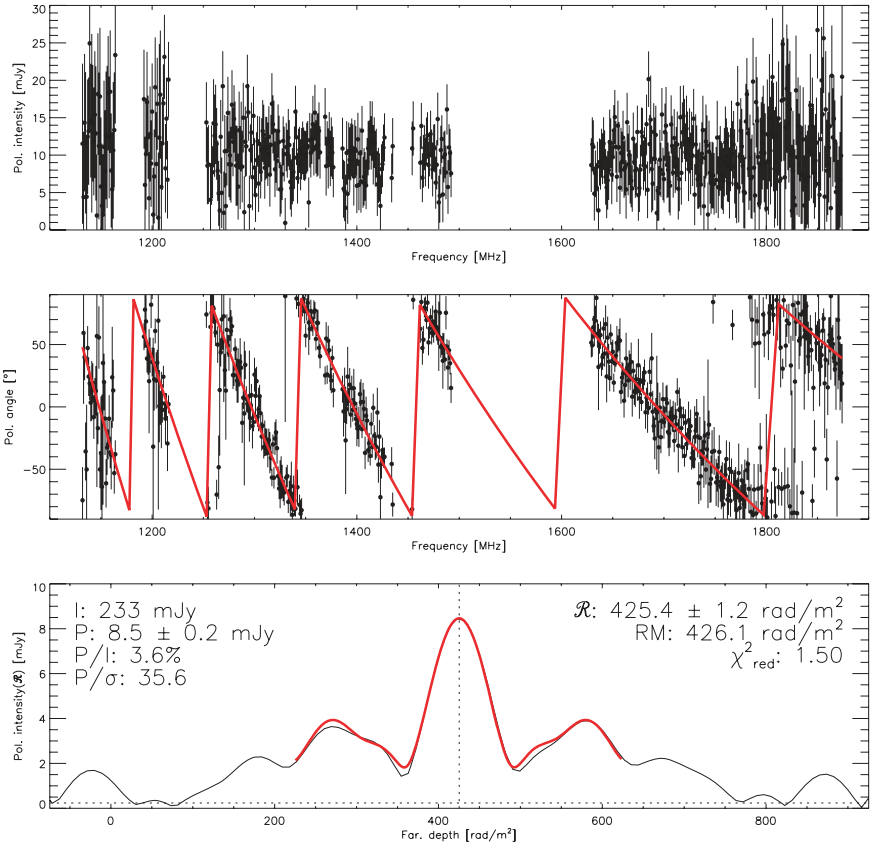

Figure 30. The polarization properties of an extragalactic source on a line of sight close to the Galactic supershell GSH287+04–17 [source coordinates: α, δ(J2000) = $10^{\rm h}\,48^{\rm m}\,07\overset{\rm s}{.}653$, $-53^\circ\,13'\,21\overset{''}{.}38$]. The top and middle panels show the polarized intensity and polarization angle as a function of frequency, which were derived from the observations. The red line in the middle panel indicates the best-fitting RM = 426 rad m^{-2} (the fit has a reduced χ^2 of 1.5). The bottom panel shows how much power (polarized intensity) is contributed by each Faraday depth. In this case 8.5 mJy is generated at a Faraday depth of 425 rad m^{-2}, which matches the average polarized intensity from the top panel and the best-fitting RM from the middle panel well. The solid red line indicates the profile that can be expected from the RM synthesis on the basis of the frequency coverage of the data. The bottom panel illustrates the strength of the RM synthesis: although polarized intensity is detected in each channel at about the 2σ level (top panel), combining all frequency channels, which is possible with RM synthesis, gives a detection with a combined polarized signal-to-noise ratio level of 36σ (bottom panel; the noise level in the bottom panel is about 0.2 mJy).

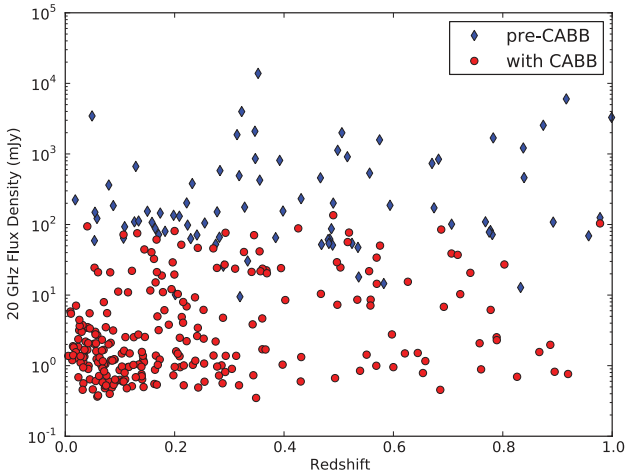

Figure 31. ATCA 20 GHz flux densities for a sample of X-ray selected QSOs against redshift. Blue diamonds indicate targets that were observed using the original correlator on the Compact Array, while red circles show the sources observed more recently using CABB. The data were obtained between 2008 and 2010 in the H168 configuration.

from its merging formation; it is not in virial equilibrium and must contain lower temperature high-pressure gas not detected in X-ray observations. Malu et al. (2011) observed the Bullet cluster (1E0657−56) at $z = 0.296$. They note that the deepest SZ features seem to avoid the regions of most intense X-ray emission (see Fig. 32). These two independent results support Malu et al.'s assertion that modelling cluster dynamics is non-trivial and that our lack of understanding of cluster merger astrophysics may be limiting our ability to model the cosmological distribution of SZ counts.

6.13 Pulsar binning

CABB is capable of operating in pulsar mode, where a pulse profile can be recorded every cycle for each frequency channel for each polarization in up to two IFs. Typically 32 phase bins across the pulsar period can be recorded with a minimum bin time of ∼110 μs.

Observations in pulsar mode require the knowledge of the pulsar rotation's period at the observatory and how the period changes over the course of the observation. This is done using a TEMPO2 predictor file (Hobbs et al. 2009) and requires that the pulsar ephemeris details are stored in the pulsar catalogue. If this is the case then the code 'psrpred' can be executed on the correlator computer to set up the predictor file.

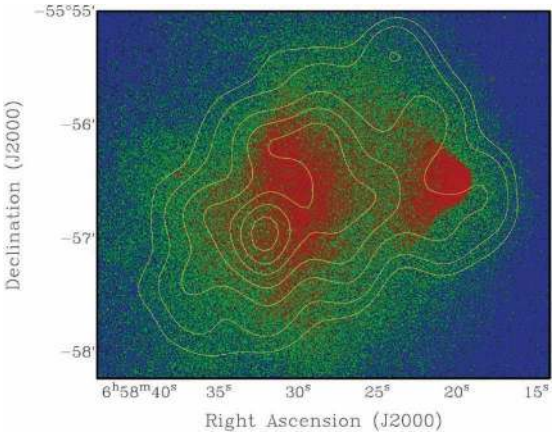

Figure 32. ATCA 18 GHz image of the SZ effect in the Bullet cluster (Malu et al. 2011) in contours overlaid on to a *Chandra* X-ray emission map displayed in colour. The hottest gas (deepest Sunyaev–Zel'dovich effect feature) is displaced from the densest regions traced by the X-ray emission (see Section 6.12). The ATCA observations were made with CABB in 2009 April (H168 array; 2 × 12 h) and 2009 June (H75 array; 3 × 8 h) using both IFs, i.e. 2 × 2 GHz bands. The Chandra X-ray Observatory is operated by the Smithsonian Astrophysical Observatory on behalf of NASA.

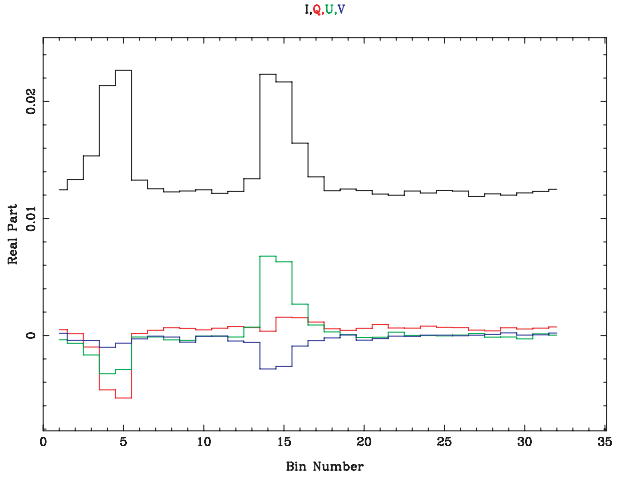

Figure 33. Observations of the pulsar PSR 1259−63 made on 2011 January 12 at a central frequency of 9.0 GHz and a total bandwidth of 2 GHz. The pulse profile is shown in 32 phase bins across the pulse period of ∼48 ms. The total intensity trace (black) shows the characteristic double peaked profile for this pulsar (Manchester & Johnston 1995). The red and green traces show Stokes Q and U, respectively; the pulsar is highly linearly polarized. Circular polarization is shown in blue.

Various science applications for pulsar mode can be conceptualized. One example is to determine where pulsars emit during the so-called off-pulse phase or whether the emission there is truly zero. A further application would be the removal of the pulsar signal to determine whether there is underlying emission from a pulsar wind nebula (Stappers, Gaensler & Johnston 1999). Finally, transient continuum (unpulsed) emission from a pulsar system can also be detected and the flux density measured without contamination from the pulsar signal (Johnston et al. 2005).

The periastron passage of the pulsar PSR B1259−63 around its companion Be star is known to produce transient emission over a wide range of wavelengths, from the radio to the TeV. The most recent periastron occurred on 2010 December 14, and a major campaign was mounted to maximize the coverage over the electromagnetic spectrum. In the radio, observations were made at the ATCA on a regular basis from early 2010 November until 2011 March using CABB in pulsar mode. Fig. 33 shows an observation made at 9 GHz on 2011 January 11. The two pulses which make up this pulsar's profile are clearly seen above a pedestal of transient emission with a flux density of ∼12 mJy. The transient emission is unpolarized. However, the pulsar itself is highly polarized (including circular polarization) as shown by the lower traces. Full analysis of these data is still in progress.

6.14 SEDs for AT20G sources observed by *Planck*

The Australia Telescope 20 GHz (AT20G) Survey (Murphy et al. 2010; Massardi et al. 2011a) used a custom-made analogue correlator, with 8 GHz of bandwidth in dual polarization, on three antennas and was completed while the CABB system was under construction. Although it had similar bandwidth to CABB, it had no delay tracking, so could not be used to follow-up sources after the survey was completed. CABB follow-up observations of 483 AT20G sources provided flux density measurements almost simultaneously with *Planck* observations (Massardi et al. 2011b). These extend the frequency coverage of *Planck* providing for the first time the instantaneous spectral energy distributions (SED) of the brightest AGN from 4.5 to 40 GHz (ATCA) and from 30 to 857 GHz (*Planck*).

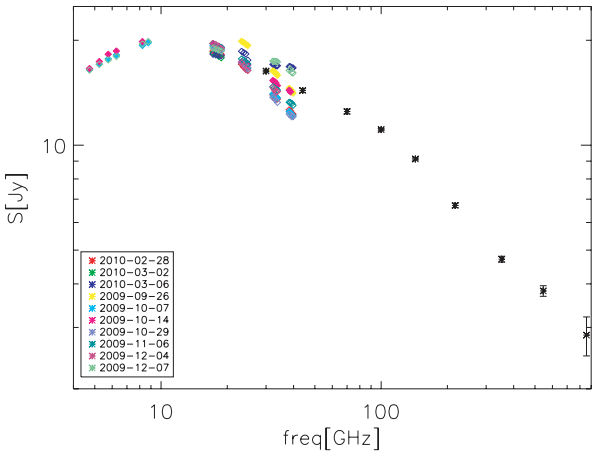

Figure 34. SED of the qusasar PKS B1921−293 as measured by the ATCA (4.5–40 GHz) over several epochs (marked with coloured open diamonds) as part of the PACO project (Massardi et al. 2011b) and by *Planck* released in the ERCSC (30–545 GHz; black asterisks, Planck collaboration 2011). Note that the displayed *Planck* flux densities were obtained from maps integrated over all scans during the satellite first sky survey (i.e. 2009 August–2010 March). Filled diamonds indicate the ATCA observing epochs within 10 d from a *Planck* scan at frequencies <100 GHz.

The project is known as the 'Planck-ATCA Co-eval Observations' (PACO). As an example we show the SED of PKS B1921−293 (also known as OV–236 or here AT20G J192451−291430), a redshift 0.35 QSO and a very bright flat spectrum AGN (see Fig. 34), often used as ATCA bandpass calibrator at mm-wavelengths. The wide-bandwidth multi-frequency CABB data sample a large fraction of the SED, up to 40 GHz, and show continuity with the Planck Early Release Compact Source Catalogue (ERCSC; Planck Collaboration 2011) data at higher frequencies. The multi-epoch CABB data highlight the importance of near simultaneous observations to sample the full SED without the distortion due to variability.

7 SUMMARY

The CABB upgrade has been described and its potential for new discoveries demonstrated. The high flexibility of CABB allows a large range of observing modes, providing wide bandwidth as well as high spectral resolution and full polarization output. The increased bandwith, effectively by a factor of 20 (from ∼100 MHz of useable bandwidth in the original correlator to the full CABB 2 GHz bandwidth), available in two IF bands (dual polarization) together with multi-bit digitization and much improved instantaneous *uv*-coverage (for continuum observations), has substantially advanced the science capabilities of the ATCA. Furthermore, the widening and combination of the original, relatively narrow 20- and 13-cm bands to one broad-band spanning 1.1 to 3.1 GHz allows multi-line (e.g. searching for H I and OH emission and absorption lines) plus continuum observations over a large range of velocities. We hope that you, the reader, will be tempted to observe with the new system if you have not already done so.

ACKNOWLEDGMENTS

The CABB project is grateful for the funding received through the Australian Government's Major National Research Facilities (MNRF) 2001 program. Our appreciation also goes to the engineers and technicians at CSIRO's Marsfield and Narrabri sites whose dedicated efforts made for the successful design, construction and implementation of this system. We thank the editor and the referee for a delightful report, improving the content and clarity of the paper.

REFERENCES

Adams T. J., Bunton J. D., Kesteven M. J., 2004, Exp. Astron., 17, 279
Artymowicz P., 1997, Ann. Rev. Earth Planet. Sci., 25, 175
Aumann H. H., 1984, BAAS, 16, 483
Bauer F. E., Dwarkadas V. V., Brandt W. N., Immler S., Smartt S., Bartel N., Bietenholz M. F., 2008, ApJ, 688, 1210
Benjamin R. A. et al., 2003, PASP, 115, 953
Beswick R. J., Muxlow T. W. B., Thrall H., Richards A. M. S., Garrington S. T., 2008, MNRAS, 385, 1143
Beuther H., Walsh A. J., Thorwirth S., Zhang Q., Hunter T. R., Megeath S. T., Menten K. M., 2007, A&A, 466, 989
Beuther H., Walsh A. J., Thorwirth S., Zhang Q., Hunter T. R., Megeath S. T., Menten K. M., 2008, A&A, 481, 169
Boccaletti A., Augereau J.-C., Baudoz P., Pantin E., Lagrange A.-M., 2009, A&A, 495, 523
Bowen M., Doherty P., Dunning A., Kanoniuk H., Moorey G., Reilly L., Sykes P., 2010, Proc. WARS, 2010, National Committee for Radio Science, Australian Academy of Science, p. 46, http://www.unisa.edu.au/itee/WARS
Brentjens M. A., De Bruyn A. G., 2005, A&A, 441, 1217
Brooks J. W., Hall P. J., Sinclair M. W., Wilson W. E., Kesteven M. J., 2000, in Dyson P., Norman R., eds, Proc. WARS 2000, National Committee for Radio Science, Australian Academy of Science, p. 182, http://www.ips.gov.au/IPSHosted/NCRS/wars/wars2000
Brooks K. J., Garay G., Mardones D., Bronfman L., 2003, ApJ, 594, L131
Brown R. L., Vanden Bout P. A., 1991, AJ, 102, 1956
Brown J. C., Haverkorn M., Gaensler B. M., Taylor A. R., Bizunok N. S., McClure-Griffiths N. M., Dickey J. M., Green A. J., 2007, ApJ, 663, 258
Bunton J. D., 2004, Exp. Astron., 17, 251
Burke-Spolaor S., Ekers R. D., Massardi M., Murphy T., Partridge B., Ricci R., Sadler E. M., 2009, MNRAS, 395, 504
Caswell J. L., Green J. A., 2011, MNRAS, 411, 2059
Caswell J. L., Haynes R. F., 1987, A&A, 171, 261
Cirasuolo M., Celotti A., Magliocchetti M., Danese L., 2003, MNRAS, 346, 447
Clark J. S., Porter J. M., 2004, A&A, 427, 839
Cooper B. F. C., 1970, Australian J. Phys., 23, 521
Coppin K. et al., 2010, MNRAS, 407, L103
Crifo F., Vidal-Madjar A., Lallement R., Ferlet R., Gerbaldi M. I., 1997, A&A, 320, L29
Curran S. J., Koribalski B. S., Bains I., 2008, MNRAS, 389, 63
Danks A. C., Wamsteker W., Shaver P. A., Retallack D. S., 1984, A&A, 132, 301
de Zotti G., Massardi M., Negrello M., Wall J., 2010, A&AR, 18, 1
DeBoer D. R. et al., 2009, Proc. IEEE, 97, 1507
Deller A. et al., 2011, PASP, 123, 275
Ekers R. D., Bell J. F., 2001, in Cohen R. J., Sullivan W. T., III, eds, Proc. IAU Symp. 196, Preserving the Astronomical Sky. Astron. Soc. Pac., San Francisco, p. 199
Ekers R. D., Whiteoak J. B., 1992, J. Electr. Electron. Eng., 12, 225
Ekers R. D., Goss W. M., Kotanyi C. G., Skellern D. J., 1978, A&A, 69, L21
Elmouttie M., Haynes R. F., Jones K. L., Sadler E. M., Ehle M., 1998, MNRAS, 297, 1202
Emonts B. H. C., Morganti R., Oosterloo T. A., Holt J., Tadhunter C. N., van der Hulst J. M., Ojha R., Sadler E. M., 2008, MNRAS, 387, 197
Emonts B. H. C. et al., 2011a, ApJ, 734, L25
Emonts B. H. C. et al., 2011b, MNRAS, 415, 665
Ferris R. H., Saunders S. J., 2004, Exp. Astron., 17, 269
Ferris R. H., Wilson W. E., 2002, URSI XXVIIth General Assembly, Maastricht, poster 1629
Frater R. H., Brooks J. W., 1992, J. Electr. Electron. Eng., 12, 100
Frater R. H., Brooks J. W., Whiteoak J. B., 1992, J. Electr. Electron. Eng., 12, 103
Freeman K., Karlsson B., Lynga G., Burrell J. F., van Woerden H., Goss W. M., Mebold U., 1977, A&A, 55, 445
Gaensler B. M., Haverkorn M., Staveley-Smith L., Dickey J. M., McClure-Griffiths N. M., Dickel J. R., Wolleben M., 2005, Sci, 307, 1610
Gordon D., 2004, in Vandenberg N. R., Baver K. D., eds, IVSG Conf. Proc. NASA/CP-2004-212255, p. 265, http://ivscc.gsfc.nasa.gov
Goss W. M., Danziger I. J., Fosbury R. A. E., Boksenberg A., 1980, MNRAS, 190, 23
Gough R., Archer J., Roberts P., Moorey G., Graves G., Bowen M., Kononiuk H., 2004, Proc. 12th GAAS Symp., p. 359
Greve T. R., Ivison R. J., Papadopoulos P. P., 2004, A&A, 419, 99
Hales C. A., Gaensler B. M., Norris R. P., Middelberg E., 2011, BAAS, 217, 142.32
Hall P. J., Brooks J. W., Sinclair M. W., Wilson W. E., Kesteven M. J., 1997, Proc. WARS 1997, p. 65, http://www.ips.gov.au/IPSHosted/NCRS/wars.html
Haverkorn M., Gaensler B. M., McClure-Griffiths N. M., Dickey J. M., Green A. J., 2006, ApJS, 167, 230
Hindson L., Thompson M. A., Urquhart J. S., Clark J. S., Davies B., 2010, MNRAS, 408, 1438
Hobbs G. et al., 2009, MNRAS, 394, 1945
Holt J., Tadhunter C. N., González Delgado R. M., Inskip K. J., Rodriguez J., Emonts B. H. C., Morganti R., Wills K. A., 2007, MNRAS, 381, 611
Hunter T. R., Brogan C. L., Megeath S. T., Menten K. M., Beuther H., Thorwirth S., 2006, ApJ, 649, 888
James G. L., 1992, J. Electr. Electron. Eng., 12, 137
James C. W., Ekers R. D., Álvarez-Muñiz J., Bray J. D., McFadden R. A., Phillips C. J., Protheroe R. J., Roberts P., 2010, Phys. Rev. D, 81, 042003
James C. W., Protheroe R. J., Ekers R. D., Álvarez-Muñiz J., McFadden R. A., Phillips C. J., Roberts P., Bray J. D., 2011, MNRAS, 410, 885
Johnston S., Ball L., Wang N., Manchester R. N., 2005, MNRAS, 358, 1069
Johnston S. et al., 2007, Publ. Astron. Soc. Australia, 24, 174
Johnston S. et al., 2008, Exp. Astron., 22, 151
Jones K. L., Koribalski B. S., Elmouttie M., Haynes R. F., 1999, MNRAS, 302, 649
Jones D. H. et al., 2009, MNRAS, 399, 683

Kellermann K. I., Sramek R., Schmidt M., Shaffer D. B., Green R., 1989, AJ, 98, 1195
Killeen N. E. B., Fluke C. J., Zhao, Jum-Hui, Ekers R. D., 1999, MNRAS, submitted (MZ381)
Klamer I. J., Ekers R. D., Sadler E. M., Weiss A., Hunstead R. W., De Breuck C., 2005, ApJ, 621, L1
Koribalski B. S., 1997, Proc. WARS 1997, p. 3, http://www.ips.gov.au/IPSHosted/NCRS/wars.html
Kramer C., Moreno R., Greve A., 2008, A&A, 482, 359
Krolik J. H., Chen W., 1991, AJ, 102, 1659
Lagrange A.-M. et al., 2010, Sci, 329, 57
Lecavelier des Etangs A. et al., 2001, Nat, 412, 706
Lonsdale C. J. et al., 2009, Proc. IEEE, 97, 1497
Mahony E. K. et al., 2010a, MNRAS, 401, 1151
Mahony E. K., Sadler E. M., Croom S. M., Ekers R. D., Feain I. J., Murphy T., 2010b, ISJKAF2010, Proc. Science Meeting, p. 72
Malu S. S., Subrahmanyan R., Wieringa M., Narasimha D., 2011, preprint (arXiv:1005.1394)
Manchester R. N., Johnston S., 1995, ApJ, 441, L65
Manchester R. N. et al., 2010, ApJ, 710, 1694
Massardi M., Ekers R. D., Ellis S., Maughan B., 2010, ApJ, 718, L23
Massardi M. et al., 2011a, MNRAS, 412, 318
Massardi M., Bonaldi A., Bonavera L., López-Caniego M., De Zotti G., Ekers R. D., 2011b, MNRAS, 415, 1597
McFadden R. et al., 2008, in Caballero R., D'Olivo J. C., Medina-Tanco G., Nellen L., Sánchez F. A., Valdés-Galicia J. F., eds, Proc. Int. Cosmic Ray Conf. Vol. 5, p. 1549
McGrath E. J., Goss W. M., De Pre C. G., 2004, ApJS, 155, 577
Middelberg E., Norris R. P., Hales C. A., Seymour N., Johnston-Hollitt M., Huynh M. T., Lenc E., Mao M. Y., 2011, A&A, 526, 8
Moorey G., Bolton R., Dunning A., Gough R., Kanoniuk H., Reilly L., 2006, Proc. WARS, R-30, http://www.ips.gov.au/IPSHosted/NCRS/wars/wars2006-meeting/index.html
Moorey G. G. et al., 2008, Proc. 38th EuMC. IEEE, New York, p. 155
Muller E. et al., 2010, ApJ, 712, 1248
Murphy T. et al., 2010, MNRAS, 402, 2403
Norris R. P. et al., 2006, AJ, 132, 2409
Orton G. S., Griffin M. J., Ade P. A. R., Nolt I. G., Radostitz J. V., 1986, Icarus, 67, 289
Papadopoulos P. P., Röttgering H. J. A., van der Werf P. P., Guilloteau S., Omont A., van Breugel W. J. M., Tilanus R. P. J., 2000, ApJ, 528, 626
Papadopoulos P., Ivison R., Carilli C., Lewis G., 2001, Nat, 409, 58
Perley R. A., Schwab, F. R., Bridle A. H., eds, 1988, ASP Conf. Ser. Vol. 6, Synthesis Imaging in Radio Astronomy. Astron. Soc. Pac., San Francisco
Perley R. et al., 2009, Proc. IEEE, 97, 1448
Planck Collaboration et al., 2011, A&A, in press (arXiv:1101.2041)
Reid M. J., Menten K. M., Zheng X. W., Brunthaler A., Xu Y., 2009, ApJ, 705, 1548
Reynolds J., 1994, ATNF Memo (AT/39.3/040)
Roberts P. P., Town G. E., 1995, IEEE Trans. Microwave Theory Tech., 43, 739
Sault R. J., 2003, ATNF Memo (AT/39.3/124)
Sault R. J., Teuben P. J., Wright M. C. H., 1995, in Shaw R. A., Payne H. E., Hayes J. J. E., eds, ASP Conf. Ser. Vol. 77, Astronomical Data Analysis Software and Systems IV. Astron. Soc. Pac., San Francisco, p. 433
Shepherd M. C., 1997, in Hunt G., Payne H. E., eds, ASP Conf. Ser. Vol. 125, Astronomical Data Analysis Software and Systems VI. Astron. Soc. Pac., San Francisco, p. 77
Sinclair M. W., Graves G. R., Gough R. G., Moorey G. G., 1992, J. Electr. Electron. Eng., 12, 147
Smith B. A., Terrile R. J., 1984, Sci, 226, 1421
Stappers B. W., Gaensler B. M., Johnston S., 1999, MNRAS, 308, 609
Taylor G. B., Carilli C. L., Perley R. A., eds, 1998, ASP Conf. Ser. Vol. 180, Synthesis Imaging in Radio Astronomy II. Astron. Soc. Pac., San Francisco
Thompson A. R., Moran J. M., Swenson G. W., Jr, 2002, Interferometry and Synthesis in Radio Astronomy, 2nd edn. Wiley, New York
Urquhart J. S., Hoare M. G., Lumsden S. L., Oudmaijer R. D., Moore T. J. T., 2008, in Beuther H., Linz H., Henning T., eds, ASP Conf. Ser. Vol. 387, Massive Star Formation: Observations Confront Theory. Astron. Soc. Pac., San Francisco, p. 381
Urquhart J. S. et al., 2010, Publ. Astron. Soc. Australia, 27, 321
van Vleck J. H., Middelton D., 1966, Proc. IEEE, 54, 2
Véron-Cetty M. P., Véron P., 2001, A&A, 375, 791
Voges W. et al., 1999, A&A, 349, 389
Voronkov M. A., Brooks K. J., Sobolev A. M., Ellingsen S. P., Ostrovskii A. B., Caswell J. L., 2006, MNRAS, 373, 411
Walsh A. J., Burton M. G., Hyland A. R., Robinson G., 1998, MNRAS, 301, 640
Walsh A. J., Thorwirth S., Beuther H., Burton M. G., 2010, MNRAS, 404, 1396
Wilner D. L., Andrews S. M., Hughes A. M., 2011, ApJ, 727, L42
Wilson W. E., Davis E. R., Loone D. G., Brown D. R., 1992, J. Electr. Electron. Eng., 12, 187
Wyatt M. C., 2008, ARA&A, 46, 339
Zuckerman B., Song Inseok, Bessell M. S., Webb R. A., 2001, ApJ, 562, L87

This paper has been typeset from a TEX/LATEX file prepared by the author.